Check for updates

ADVANCING EARTH AND SPACE SCIENCES

Geochemistry, Geophysics, Geosystems

RESEARCH ARTICLE
10.1029/2025GC012175

Mantle Source Evolution Along the South Atlantic Transect (31°S) Records a Transition From HIMU Plume Component to Depleted MORB

P. D. Kempton[1], R. M. Coggon[2], I. Millar[3], T. M. Belgrano[4], E. Albers[5], A. Michalik[2], J. A. Milton[2], A. D. Evans[2], R. N. Taylor[2], and D. A. H. Teagle[2]

[1]Department of Geology, Kansas State University, Manhattan, KS, USA, [2]University of Southampton, School of Ocean and Earth Science, National Oceanography Centre, Southampton, UK, [3]British Geological Survey, Nottinghamshire, UK, [4]University College Dublin, School of Earth Sciences, Dublin, Ireland, [5]Alfred Wegener Institute, Helmholtz Centre for Polar and Marine Research, Bremerhaven, Germany

Key Points:

- IODP drill sites reveal changes in source composition over time along a 61-million-year flowline on the western mid-Atlantic Ridge (MAR) (~31°S)
- Basement <49 Ma is tholeiitic and isotopically similar to MORB; older basalts (~61 Ma) range from MORB-like to OIB-like alkali basalts
- Sr-Nd-Pb-Hf isotopes support first-reported occurrence of a HIMU component in this region of the MAR

Supporting Information:

Supporting Information may be found in the online version of this article.

Correspondence to:

P. D. Kempton,
pkempton@ksu.edu

Citation:

Kempton, P. D., Coggon, R. M., Millar, I., Belgrano, T. M., Albers, E., Michalik, A., et al. (2025). Mantle source evolution along the South Atlantic Transect (31°S) records a transition from HIMU plume component to depleted MORB. *Geochemistry, Geophysics, Geosystems*, *26*, e2025GC012175. https://doi.org/10.1029/2025GC012175

Received 14 JAN 2025
Accepted 20 MAR 2025

Author Contributions:

Conceptualization: P. D. Kempton
Data curation: P. D. Kempton
Formal analysis: P. D. Kempton
Funding acquisition: P. D. Kempton
Investigation: P. D. Kempton, I. Millar, T. M. Belgrano, E. Albers, A. Michalik, J. A. Milton, A. D. Evans
Methodology: P. D. Kempton
Project administration: P. D. Kempton
Resources: P. D. Kempton, R. M. Coggon
Visualization: P. D. Kempton

© 2025 The Author(s). Geochemistry, Geophysics, Geosystems published by Wiley Periodicals LLC on behalf of American Geophysical Union.
This is an open access article under the terms of the Creative Commons Attribution License, which permits use, distribution and reproduction in any medium, provided the original work is properly cited.

Abstract

Interactions between mantle plumes and mid-ocean ridges create considerable spatial variation in composition along ridge axes. What is less well known is the temporal variation in MORB compositions along single mantle flow lines. IODP Expeditions 390/393/390C/395E recovered basaltic basement from seven sites along a flow line, the South Atlantic Transect (SAT), on the western flank of the mid-Atlantic Ridge (MAR) at ~31°S. SAT basalts ≤49 Ma are tholeiitic with isotopic compositions similar to MORBs from the MAR between 25° and 28°S. Basement from the oldest SAT site (U1556; 61.2 Ma) is more complex, consisting of three stratigraphic sequences (SSA, SSB and SSC) ranging from MORB-like at the bottom (SSC) to Ocean Island Basalt (OIB)-like at the top (SSA); their isotopic compositions are distinct relative to both younger SAT basalts and the EM1-type Tristan–Gough plume that dominates the region, being more akin to HIMU. The presence of previously unrecognized HIMU mantle in this region is due to one or more ridge jumps that occurred west of the Walvis Ridge at ~65 Ma. These ridge jumps relocated the spreading axis over a portion of the HIMU plume that had previously given rise to late-stage, off-axis HIMU magmatism adjacent to the Walvis Ridge. Upwelling beneath the spreading center progressively tapped a variably depleted source, reproducing it in reverse in the volcanic stratigraphy at Site U1556. Continued upwelling beneath the spreading center removed most of the HIMU plume material within ~12 Myr, the time of Site U1558 (49.2 Ma).

Plain Language Summary

Oceanic basalts provide a window into Earth's upper mantle, its composition and the processes that have shaped it. Decades of research have shown that there is considerable compositional variation along mid-ocean ridges as a consequence of deep mantle plumes, which variably interact with the ridge system. However, there have been few opportunities to explore how mantle source composition varies in a single location over time. The South Atlantic Transect, an array of IODP drill sites aligned along a single flow line on the western flank of the Mid-Atlantic Ridge at ~31°S, provides one such opportunity to explore this aspect of mantle evolution. New compositional data for basalts recovered during IODP Expeditions 390/393/390C/395E reveal changes in source composition over the 61-million-year flow line sampled by the transect. Basaltic basement <49 Ma is compositionally similar to depleted mid-ocean ridge basalts from ridge segments to the north. In contrast, the oldest basalts (~61 Ma) are compositionally diverse and include alkali basalts typical of plume magmatism but isotopically distinct from the Tristan-Gough plume system previously thought to have dominated the region since the opening of the South Atlantic.

1. Introduction

Evidence in support of the newly emerging theory of plate tectonics came in 1969 when Leg 3 of the Deep Sea Drilling Project (DSDP) drilled a series of holes across the ocean floor between South America and Africa (Maxwell et al., 1970). Their results, which showed that oceanic crust becomes progressively older away from the ridge, ushered in a new paradigm that transformed how geoscientists view the way the Earth works.

Although Leg 3 corroborated Alfred Wegner's theory about the breakup of the Gondwana supercontinent, the mechanism driving continental breakup and the role of mantle plumes remain contested (Niu, 2020, and references therein). The Tristan—Gough plume system is arguably one of the best examples supporting an association between plume magmatism and continental breakup (Class & le Roex, 2011; Taposeea et al., 2017), but the details

Writing – original draft: P. D. Kempton, R. M. Coggon, T. M. Belgrano, E. Albers, A. Michalik, J. A. Milton, A. D. Evans, R. N. Taylor, D. A. H. Teagle
Writing – review & editing: P. D. Kempton, R. M. Coggon, I. Millar, T. M. Belgrano, E. Albers, A. Michalik, J. A. Milton, A. D. Evans, R. N. Taylor, D. A. H. Teagle

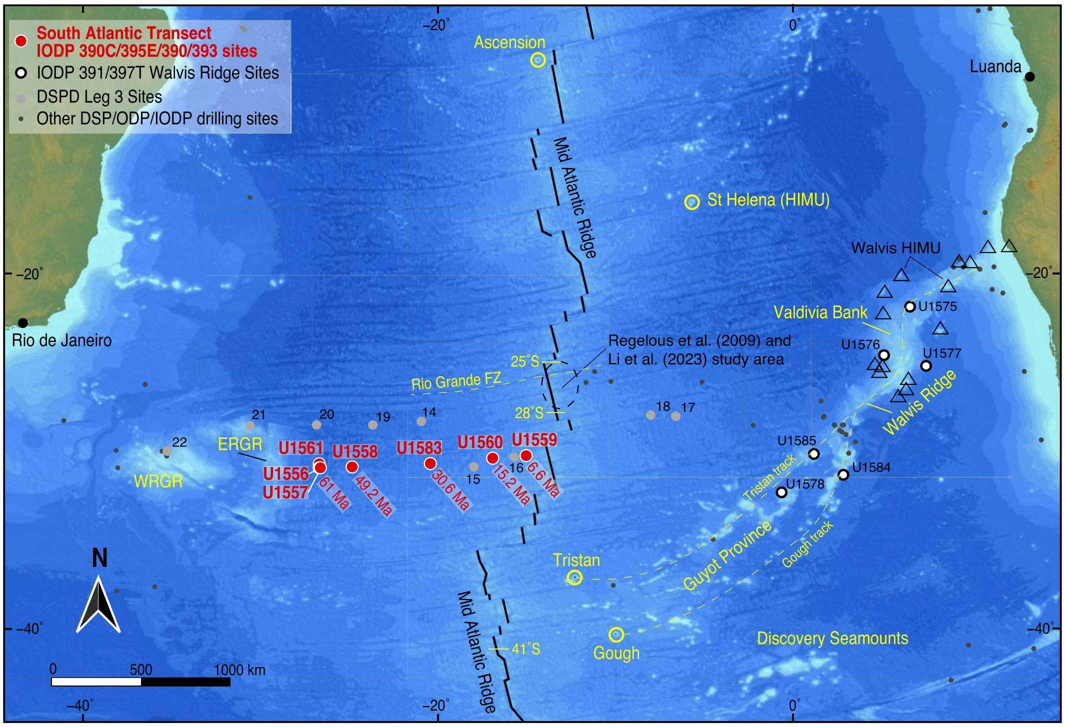

Figure 1. Location and tectonic setting of the South Atlantic Transect drill sites. Locations of the SAT and Leg 3 drill sites are shown as red and brown circles, respectively. Approximate trace of the Mid-Atlantic Ridge is shown as a solid black line. Sites drilled during IODP Expeditions 391 and 397T along the Walvis ridge are shown as white dots; other DSDP, ODP, and IODP drill sites are shown as small black dots. Late Walvis ridge seamounts with HIMU component are shown as black triangles (Homrighausen et al., 2020). WRGR, western Rio Grande Rise; ERGR, eastern Rio Grande Rise. The study area for on-axis MORBs from Regelous et al. (2009) and Li et al. (2023) is outlined by a black dashed line. GEBCO Compilation Group (2024) GEBCO 2024 Grid (https://doi.org/10.5285/1c44ce99-0a0d-5f4f-e063-7086abc0ea0f). IODP site locations from here: https://iodp.tamu.edu/scienceops/maps.html.

of breakup, particularly in its earliest stages, and implications for evolution of the underlying mantle remain uncertain.

More than 50 years after DSDP Leg 3, International Ocean Discovery Program (IODP) Expeditions 390, 393, 393C, and 395E (Figure 1) drilled a transect of holes across the western flank of the southern Mid-Atlantic Ridge (MAR) at ~31°S in crust ranging from ~61.2 to 6.6 Ma (Coggon et al., 2024) less than ~300 km south of the Leg 3 drill sites. This new South Atlantic Transect (SAT) provides an opportunity to answer new and more in-depth questions about the process of opening the South Atlantic. In this study, we focus on two first-order questions.

1. Has plume magmatism left a lasting impact on the composition of the upper mantle in the region of the South Atlantic Transect?
2. How have any such compositional impacts changed over time, and what does that tell us about the dynamics of the underlying mantle during progressive opening of the Atlantic?

2. Background

2.1. Opening of the South Atlantic

Breakup of the Gondwana supercontinent in the Cretaceous led to the formation of the South Atlantic Ocean basin (Class & le Roex, 2011; Fromm et al., 2015; Gassmöller et al., 2016; Seton et al., 2012; Taposeea et al., 2017; Torsvik et al., 2009). Coincident with this breakup, at ~132 Ma, was the arrival of the Tristan-Gough plume head (Renne et al., 1996). This produced two large igneous provinces (LIPs): the Paraná on the South American continent and its conjugate, the Etendeka, on the African continent (Morgan, 1971; Peate, 1997; Renne et al., 1996). Between ~120 and 80 Ma, magmatism associated with the plume tail formed the Rio Grande Rise (RGR) on the west of the present day ridge and the Walvis Ridge on the east (Class & le Roex, 2011; Cliff

15252027, 2025, 4, Downloaded from https://agupubs.onlinelibrary.wiley.com/doi/10.1029/2025GC012175 by British Geological Survey, Wiley Online Library on [19/05/2025]. See the Terms and Conditions (https://onlinelibrary.wiley.com/terms-and-conditions) on Wiley Online Library for rules of use; OA articles are governed by the applicable Creative Commons License

15252027, 2025, 4, Downloaded from https://agupubs.onlinelibrary.wiley.com/doi/10.1029/2025GC012175 by British Geological Survey, Wiley Online Library on [19/05/2025]. See the Terms and Conditions (https://onlinelibrary.wiley.com/terms-and-conditions) on Wiley Online Library for rules of use; OA articles are governed by the applicable Creative Commons License

et al., 1991; Gibson et al., 2005; Hoyer et al., 2022; Humphris & Thompson, 1983; le Roex et al., 1990; O'Connor & Jokat, 2015; Richards et al., 1989; Richardson et al., 1982; Rohde et al., 2013; Seton et al., 2012). Petrogenesis of the Rio Grande Rise remains controversial (Hoyer et al., 2022, and references therein), but it includes at least two distinct regions, the Western Rio Grande Rise (WRGR) and the Eastern Rio Grande Rise (ERGR) (Figure 1). Geochemical data are consistent with Tristan-Gough plume contributions to the magmatic products on both east and west RGR as well as the Walvis Ridge (Class et al., 2023; Gibson et al., 2005; Hoernle et al., 2015; Homrighausen et al., 2019). Geophysical and petrological data have been interpreted by some as evidence for incorporation of a continental fragment, detached from the margin of Brazil, in the WRGR, although not in the ERGR (Mohriak et al., 2010; Santos et al., 2019; Ussami et al., 2013). However, more recent geochemical studies (Homrighausen et al., 2023; Hoyer et al., 2022) argue against the presence of detached continental crust in either east or west RGR.

Between ~93 and 68 Ma, the plume was co-located with a spreading center that was propagating southward, forming first Valdivia Bank, now located on the African plate, and subsequently the N-S oriented eastern RGR, which is on the South American plate (Davidson et al., 2023; Homrighausen et al., 2023; O'Connor & Jokat, 2015; Rohde et al., 2013; Sager et al., 2021). After ~68 Ma, a sequence of ridge jumps separated the RGR from the Walvis Ridge (Graça et al., 2019; Thoram et al., 2019). This temporarily terminated magmatic activity on the South American plate and confined plume volcanism to the African plate, generating what is referred to as the Guyot Province. This portion of the Tristan-Gough hotspot track consists of at least two age-progressive, and isotopically distinct, volcanic tracks, one terminating in the ocean island of Tristan da Cunha and the other ending at Gough Island (Homrighausen et al., 2023; Hoyer et al., 2022; O'Connor & Jokat, 2015; Rohde et al., 2013).

Previous studies of mid-ocean ridge basalt (MORB) in the South Atlantic suggest there are major compositional variations along the length of the ridge axis (Agranier et al., 2005; Class & le Roex, 2011; Li et al., 2023; Regelous et al., 2009; Stracke et al., 2022). Basalts north of ~25°S tend to have normal (NMORB) compositions, whereas those to the south are unusually enriched in incompatible trace elements and have distinct isotopic compositions that have been referred to as the DUPAL anomaly (Class & le Roex, 2011), defined by elevated $^{87}Sr/^{86}Sr$ ratios and high $^{208}Pb/^{204}Pb$ and $^{207}Pb/^{204}Pb$ for a given $^{206}Pb/^{204}Pb$ relative to the Northern Hemisphere Reference Line (NHRL) (Hart, 1984). The origin of the DUPAL anomaly is controversial, but an association with plumes originating in the deep mantle is generally accepted (Class & le Roex, 2011; Homrighausen et al., 2019; Schwindrofska et al., 2016), although contamination of the upper oceanic mantle by delamination of dense lower continental crust (± lithospheric mantle) during continental rifting has not been entirely ruled out (Regelous et al., 2009).

2.2. Summary of the South Atlantic Transect and Study Samples

The South Atlantic Transect (SAT) comprises seven sites, the oldest of which is only about 200 km from the ERGR (Figure 1). Crustal ages for each site were calculated from magnetic data acquired during the CREST cruise (Kardell et al., 2019), prior to drilling, and are consistent with both the biostratigraphic and magneto-stratigraphic ages of the basal sediments overlying the crust (Coggon et al., 2024). Because of limited basement penetration at Site U1561 (<3 m), we have omitted it from this study. Details of spreading rates, core recovered, core recovery rate, and lithologic units for the remaining six SAT sites summarized below are from Coggon et al. (2024). Additional details on petrology, petrography, geochemistry, and physical properties are available there.

With one exception, explained below, all samples used in this study are hand-picked fresh basaltic glasses. Therefore, sampling locations were dictated by the intervals where fresh glass was available. Nonetheless, our sampling strategy aimed to cover as much of the original, unaltered, variation in basalt composition as possible.

The location of each study sample within the basement is indicated in Figure 2, a plot of $(TiO_2/Y)*100$ versus depth at each site. The compositional data used in this diagram are from direct analysis of the core by portable XRF (pXRF) (Jonnalagadda et al., 2024). Note that the pXRF analytical campaign did not target the freshest material. Instead, the purpose was to provide representative compositional information for the core material recovered whether that be altered or fresh. We have therefore chosen to represent the compositional variation across all six sites using $(TiO_2/Y)*100$ because (a) Ti and Y are relatively immobile elements during seawater alteration (Pearce, 2008) and (b) they are reasonably well determined by handheld XRF (~5% total error and precision; Jonnalagadda et al., 2024).

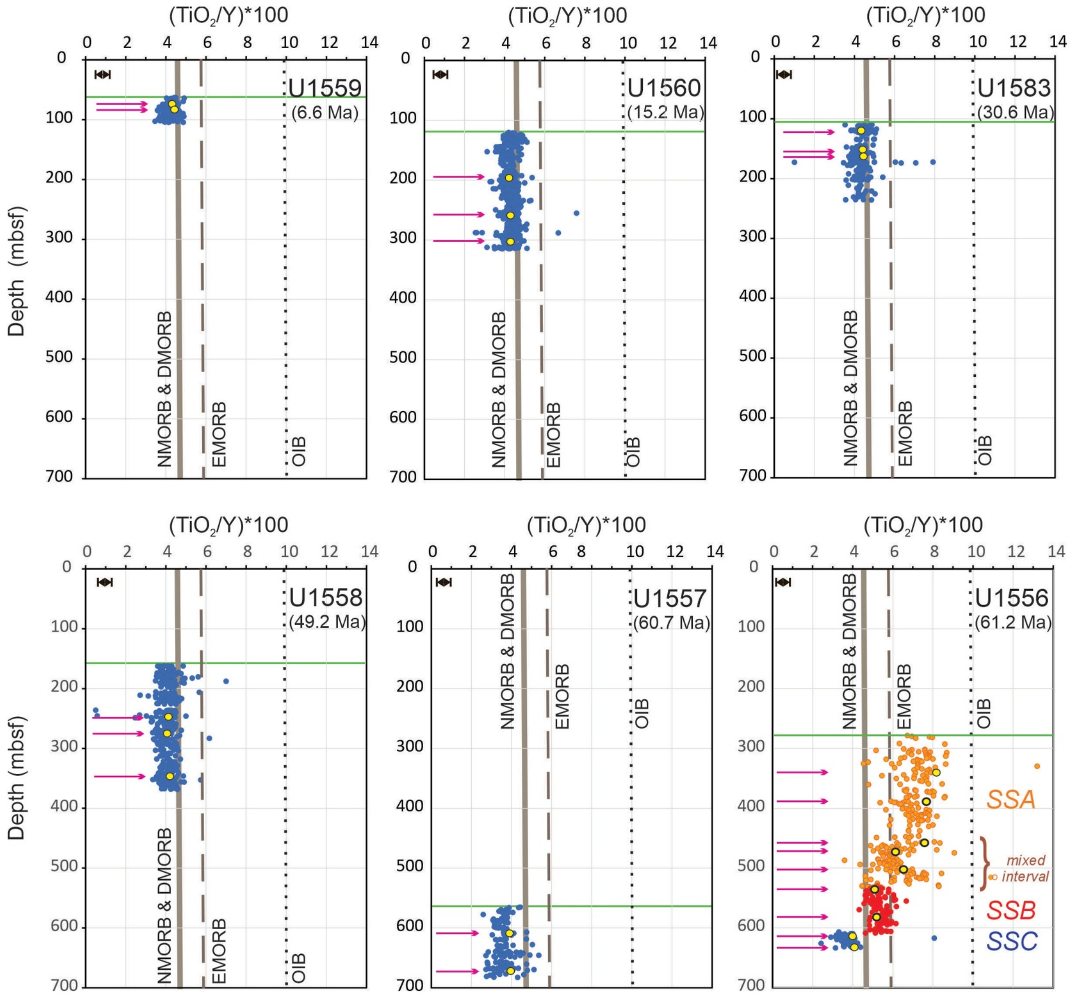

Figure 2. Plot of $(TiO_2/Y)*100$ versus depth (meters below seafloor, mbsf). Compositional data are from direct analysis of the core by portable XRF (pXRF) (Jonnalagadda et al., 2024). Tholeiitic basalts from Sites U1559, U1560, U1583, U1558, and U1557 are shown as blue dots. The three stratigraphic sequences from Site U1556 are distinguished as follows: orange dots for SSA, red dots for SSB, and blue dots for SSC. To aid in comparison, all diagrams are plotted to the same scale, regardless of the depths to the top and bottom of the basement at each site. The sediment—basement interface is indicated by horizontal green lines. Shown for comparison are the average compositions for NMORB to DMORB, which are similar for this parameter and shown as thick gray vertical lines, and EMORB (dashed gray lines) from Gale et al. (2013). Average composition for Ocean Island Basalt (OIB) (dotted gray lines) from Sun and McDonough (1989). Black double-headed arrows indicate approximate analytical uncertainty on individual measured ratios (see Jonnalagadda et al., 2024, for details). Pink arrows denote the locations of samples for this study; $(TiO_2/Y)*100$ values for these samples, determined by ICPMS (see Methods, Supporting Information S1), are shown as yellow-filled circles.

Site U1559—The easternmost and youngest (~6.6 Ma) site along the SAT. Located on a crust that is 5.6 km thick (Christeson et al., 2020) formed at a half spreading rate of 17 mm/yr. Drilling penetrated 44 m sub-basement at Hole U1559B and recovered 12.73 m for an average recovery of 29%. The rocks were divided into five lithological units, four of which are slightly to moderately altered basalts and one is a thin layer of indurated calcareous sediment. The basalts recovered are predominantly aphyric to sparsely plagioclase phyric pillow lavas and flows. Figure 2 shows limited compositional variation at Site U1559, and all samples appear to have NMORB to DMORB compositions within the uncertainty of the pXRF data. We have analyzed two samples from this site: 393-U1559B-5R-1, 26–30 cm and 393-U1559B-7R-1, 0–5 cm. Glass recovery at Site U1559 was limited, so glass sample 393-U1559B-7R-1, 0–5 cm has been supplemented by one whole rock sample, 393-U1559B-5R-1, 26–30 cm, selected for its freshness (Table S1).

15252027, 2025, 4, Downloaded from https://agupubs.onlinelibrary.wiley.com/doi/10.1029/2025GC012175 by British Geological Survey, Wiley Online Library on [19/05/2025]. See the Terms and Conditions (https://onlinelibrary.wiley.com/terms-and-conditions) on Wiley Online Library for rules of use; OA articles are governed by the applicable Creative Commons License

Site U1560—Located on ~15.2 Ma crust that is ~5.6 km thick (Christeson et al., 2020) formed at a half spreading rate of 25.5 mm/yr. Drilling penetrated 192 m sub-basement and recovered 75 m of volcanic basement at Hole U1560B for an average recovery of 39%. The rocks were divided into six lithological units. The recovered basalts are predominantly aphyric to moderately plagioclase-olivine-augite phyric pillow lavas and lesser sheet and massive flows. Evidence of low temperature hydrothermal alteration by seawater-derived fluids in the form of clay, zeolite, carbonate, and iron oxyhydroxide secondary minerals is present in whole rock material throughout, but fresh (unaltered) glass was also recovered. Figure 2 shows that compositional variation at Site U1560 is comparable to that at Site U1559, with data clustering around the NMORB—DMORB average compositions. Three glass samples have been analyzed: 393-U1560B-17R-1, 62–68 cm, 393-U1560B-30R-1, 0–4 cm, and 393-U1560B-39R-1, 7–13 cm.

Site U1583—Located on ~30.6 Ma oceanic crust that is ~7 km thick (Christeson et al., 2020) formed at a half spreading rate of 24 mm/yr. Drilling penetrated ~130 m sub-basement and recovered 45.79 m of slightly to moderately altered volcanic basement, with an average recovery of 35%. The rocks were divided into seven volcanic and intra-volcanic breccia lithologic units and subsequently grouped into three eruptive sequences (A, B, and C) separated by two intervals of sedimentary breccias. These breccias contain angular basalt and glass clasts from the underlying volcanic units and are interpreted as having been deposited during periods of eruptive hiatus. Sequence A consists primarily of aphyric to moderately plagioclase - olivine phyric pillow basalts and flows; Sequence B consists of moderately plagioclase - olivine ± augite phyric pillow lavas; Sequence C consists mostly of aphyric to sparsely plagioclase-olivine phyric pillow lavas. The basalts have secondary mineralogy typical of low temperature hydrothermal alteration by seawater. Compositional variation at Site U1583 is broadly similar to that at Sites U1559 and U1560, clustering around the NMORB—DMORB average compositions (Figure 2). Three glass samples have been analyzed: Samples 393-U1583F-5R-3, 82–84 cm and 393-U1583F-12R-1, 79–82 cm are from different units within eruptive sequence A; Sample U1583F-14R-1, 82–85 cm is from eruptive sequence B.

Site U1558—Located on ~49.2 Ma oceanic crust that is 5.5 km thick (Christeson et al., 2020) and formed at a half spreading rate of 19.5 mm/yr. Drilling penetrated ~204 m sub-basement and recovered 97.5 m of volcanic basement, with an average recovery rate of 48%. The rocks were divided into five volcanic and intra-volcanic units, subsequently grouped into two eruptive sequences (A and B) separated by a sedimentary breccia ~1 m thick. Sequence A consists of highly plagioclase—olivine—clinopyroxene phyric pillow basalts and flows. The pyroxene in this sequence is notably green in the hand sample, which contrasts with the black augite phenocrysts present at most other SAT sites. Sequence B consists of plagioclase—olivine phyric pillow basalts and flows. The basaltic rocks are moderately to highly altered by interaction with seawater-derived fluids, but some fresh glass is preserved. Compositional variation at Site U1558 is similar to that at Sites U1559, U1560, and U1583, although most samples from this site have lower TiO_2/Y ratios than DMORB (Figure 2). Three glass samples were analyzed from this site: 393-U1558D-15R-3, 37–40 cm; 393-U1558D-20R-2, 44–49 cm; 393-U1558D-35R-1, 34–41 cm. All samples are from eruptive sequence B. Given the compositional similarity between Sequences A, B and C (Figure 2), we do not view this as a sampling bias for this site.

Site U1557—Located on ~60.7 Ma basement that is ~3.6 km thick and formed at a half spreading rate of ~13.5 mm/yr (Christeson et al., 2020). Drilling recovered 71.3 m of basement, with an average recovery rate of 65%. However, all basement rocks recovered are breccias from a sedimentary talus deposit consisting of moderately to highly altered pillow basalt clasts variously cemented by carbonates and zeolites. Fresh glass is rare but retained on a few clasts. All basement cores were grouped into a single lithological unit due to the lack of systematic variation downhole. Two glass samples were analyzed from this site: 390-U1557D-6R-2, 95–100 cm and 390-U1557D-13R-6, 86–89 cm. Compositional variation is similar to that at Site U1558, with TiO_2/Y ratios lower than DMORB (Figure 2).

Site U1556—Westernmost site in the transect, located ~6.5 km west of Site U1557 and ~200 east of the ERGR. Crustal age is ~61.2 Ma, crustal thickness is ~3.6 km, and the half spreading rate is ~13.5 mm/yr (Christeson et al., 2020). Drilling penetrated ~350 m sub-basement in which the average recovery rate was relatively high (~56%) and yielded 192 m of variably altered basalts divided into 13 lithologic units, grouped into three compositionally distinct stratigraphic sequences.

15252027, 2025, 4, Downloaded from https://agupubs.onlinelibrary.wiley.com/doi/10.1029/2025GC012175 by British Geological Survey, Wiley Online Library on [19/05/2025]. See the Terms and Conditions (https://onlinelibrary.wiley.com/terms-and-conditions) on Wiley Online Library for rules of use; OA articles are governed by the applicable Creative Commons License

10.1029/2025GC012175

Stratigraphic Sequence A (SSA; orange dots in Figure 2) includes Lithologic Units 1–11. These rocks are alkalic (Coggon et al., 2024) and OIB-like, as suggested by their high TiO_2/Y ratios. They consist primarily of sparsely to moderately olivine phyric basalt pillow lavas that are moderately to highly altered throughout. Below ∼240 m sub-basement (∼420 mbsf, meters below seafloor), SSA is observed crosscutting the underlying Stratigraphic Sequence B (SSB), which is also apparent in the compositional shift to lower TiO_2/Y ratios toward the bottom of SSA (Figure 2). We have analyzed five samples from SSA: 390-U1556B-11R-1, 23–26 cm; 390-U1556B-18R-1, 40–43 cm; 390-U1556B-25R-1, 121–123 cm; 390-U1556B-28R-2, 28–32 cm; and 390-U1556B-33R-3, 64–71 cm. Samples 390-U1556B-11R-1, 23–26 cm and 390-U1556B-18R-1, 40–43 cm are stratigraphically above the interval of crosscutting relationships and represent the "purest" examples of SSA. Samples 390-U1556B-25R-1, 121–123 cm; 390-U1556B-28R-2, 28–32 cm; and 390-U1556B-33R-3, 64–71 cm are from the mixed interval; their compositions overlap that of EMORB in terms of TiO_2/Y ratios, although all the glasses analyzed from this interval are alkalic (see Results below).

Stratigraphic Sequence B (red dots in Figure 2) consists of Unit 12 and contains aphyric to very sparsely olivine (micro)phyric basalts that are highly altered to various shades of brown to reddish orange. They are compositionally intermediate between EMORB and NMORB in terms of TiO_2/Y, but all are subalkaline tholeiites (see Results below). We have analyzed two glass samples from SSB: 390-U1556B-39R-2, 109–116 cm and 390-U1556B-49R-1, 27–32 cm.

Stratigraphic Sequence C (blue dots in Figure 2) consists of Lithologic Unit 13. The rocks are distinctive in being highly plagioclase-olivine-pyroxene phyric; the pyroxene is green rather than black, indicative of diopside rather than augite. The lavas are also distinctive in that, rather than pillow lavas, they erupted as thick, massive lava flows that integrated layers of pelagic sediment into their chilled margins, suggesting a period of volcanic hiatus prior to the onset of magmatism. The basalts are slightly to moderately altered. We have analyzed two glass samples from SSC: 390-U1556B-55R-3,28–31 cm and 390-U1556B-59R-3, 136–141 cm. Like the basalts from U1557, TiO_2/Y ratios suggest compositions that are more depleted than DMORB (Figure 2).

3. Results

3.1. Major and Trace Elements

Basement rocks from Sites U1559, U1560, U1583, U1558, U1557, U1556 SSB, and U1556 SSC are all subalkaline tholeiitic basalts typical of MORB (Figure 3), as shown on a plot of Total Alkalis versus Silica (TAS) [Note: Information on analytical methods is provided in Text S1 in Supporting Information S1]. In contrast, the rocks of Stratigraphic Sequence A (SSA), from the top of Hole U1556B, plot on or above the alkaline—subalkaline boundary of Macdonald and Katsura (1964). Moreover, the data form a linear array that extends from the trachybasalt field toward the tholeiitic basalts from underlying Stratigraphic Sequence, SSB. Within this array, the most alkalic compositions are from the top of Hole 1556B, whereas the least alkalic samples are those from the interval where SSA basalts are observed intruding SSB (see Background).

MgO contents of the measured SAT glasses range from 9.15 to 6.32 wt.%, with Mg numbers [molar Mg/(Mg + 0.9Fe)] ranging from 67 to 60 (Table S1). High Ni contents (>120 ppm) are observed in tholeiites from Site U1557 and U1556 SSB as well as one alkali basalt from SSA (Table S1). However, the most primitive samples, with Mg numbers of 66–67 and high Ni, are those from Site U1557, as well as one sample from eruptive sequence B from Site U1558.

The concentrations of most major and trace elements correlate poorly with indices of fractionation, such as MgO and Mg number (Figure S1 in Supporting Information S1), indicating that multiple parental magma compositions are required across the transect. Notably, most SAT tholeiites have higher MgO, CaO, and Cr, as well as lower TiO_2, Na_2O, and K_2O than the NMORB and DMORB averages of Gale et al. (2013) (Figure S1 in Supporting Information S1). Indeed, all basalt glasses analyzed in this study from Sites U1558 and younger (i.e., ≤49.2 Ma)—hereafter referred to as the younger SAT sites—have K_2O contents that are even lower than DMORB (<0.096 wt. %) (Table S1). In contrast, the lowest Na_2O (1.85–1.93 wt. %) and TiO_2 (0.85–0.98 wt. %) contents are observed in tholeiites from the oldest sites, U1557 and U1556 SSC (Figure S1 in Supporting Information S1).

Incompatible trace element variations are summarized in multi-element plots normalized to the median NMORB value of Gale et al. (2013) (Figure 4). The significantly lower concentrations of elements on the left side of the diagrams, those with normalized values <1, show that basalts from Sites U1559, U1560, U1583, and to some

15252027, 2025, 4, Downloaded from https://agupubs.onlinelibrary.wiley.com/doi/10.1029/2025GC012175 by British Geological Survey, Wiley Online Library on [19/05/2025]. See the Terms and Conditions (https://onlinelibrary.wiley.com/terms-and-conditions) on Wiley Online Library for rules of use; OA articles are governed by the applicable Creative Commons License

15252027, 2025, 4, Downloaded from https://agupubs.onlinelibrary.wiley.com/doi/10.1029/2025GC012175 by British Geological Survey, Wiley Online Library on [19/05/2025]. See the Terms and Conditions (https://onlinelibrary.wiley.com/terms-and-conditions) on Wiley Online Library for rules of use; OA articles are governed by the applicable Creative Commons License

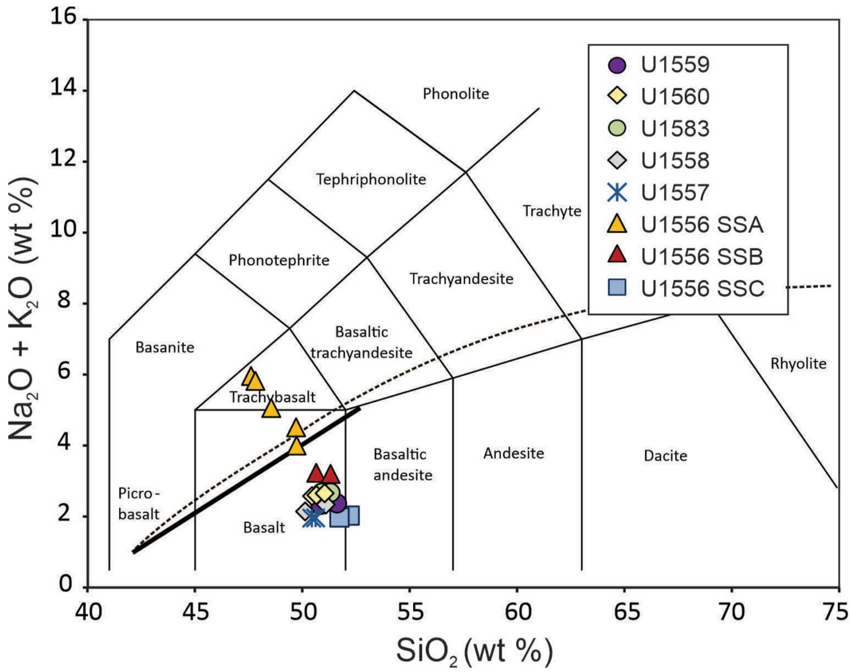

Figure 3. Plot of total alkalis versus SiO_2 for SAT basalts. The solid black line is the alkalic-tholeiitic dividing line for Hawaiian basalts from Macdonald and Katsura (1964); the dashed curve is the boundary from Miyashiro (1978).

extent U1558 are unusually depleted in the most incompatible trace elements relative to this estimate of NMORB globally (Figures 4a–4d). Rubidium and Ba contents, for example, are nearly an order of magnitude lower for Sites U1559 and U1560 than NMORB. In contrast, the less incompatible elements, for example, Zr to Lu, show relatively flat patterns near a value of 1. An interesting feature of the data, however, is that the degree of depletion is greatest among the younger basalts from Sites U1559, U1560 and U1583; the 49-million-year-old basalts from Site U1558 are also depleted, but less so.

In contrast, the older tholeiites from Sites U1557 and U1556 SSC show an unusual concave upward pattern (Figures 4e and 4f). Most elements have NMORB-normalized values less than one, but there is a distinct minimum in the middle range of incompatible elements (those between La and Hf), suggesting re-enrichment of a previously depleted source (see below). The enrichment observed in the most incompatible elements is even greater for U1556 SSB tholeiites, although the pattern is flat and around a value of one for the less incompatible elements to the right of Zr (Figure 4g). The alkalic basalts from the top of Hole U1556B (SSA) show the greatest degree of incompatible element enrichment, although even these basalts exhibit a relatively flat pattern for the heaviest rare earth elements (i.e., Dy to Lu) (Figure 4h).

3.2. Isotopes

Results for Sr, Nd, Pb, and Hf isotopes are reported in Table S2 and summarized in Figure 5. For εNd versus initial $^{87}Sr/^{86}Sr$ (Figure 5a), the SAT basalts plot within or near the fields for South Atlantic MORB from the modern ridge axis. South Atlantic MORBs are known to be compositionally diverse (Agranier et al., 2005; Douglass et al., 1999; Fontignie & Schilling, 1996; Schilling et al., 1985), so we focus our comparisons on the ridge segments that border the SAT transect and consider two distinct regions. Basalts from 25° to 28°S represent a region distant from plume influence (Li et al., 2023; Regelous et al., 2009), whereas those that erupted between 28° and 41°S are from a region where interactions with the Tristan-Gough plume are recognized (Class & le Roex, 2011). As a result, MORBs between 25° and 28°S have more depleted (i.e., higher) εNd values (>7.8), whereas those from south of 28°S exhibit a much wider range of compositions extending to εNd values as low as 2.6. SAT basalts from Sites U1559 and U1560 and two of the three samples from Site U1583 plot within the more depleted South Atlantic MORB field (25°–28°S). In contrast, older SAT tholeiites plot within or near the field of plume-influenced South Atlantic MORB (28°–41°S). The alkalic basalts, U1556 SSA, and enriched tholeiites,

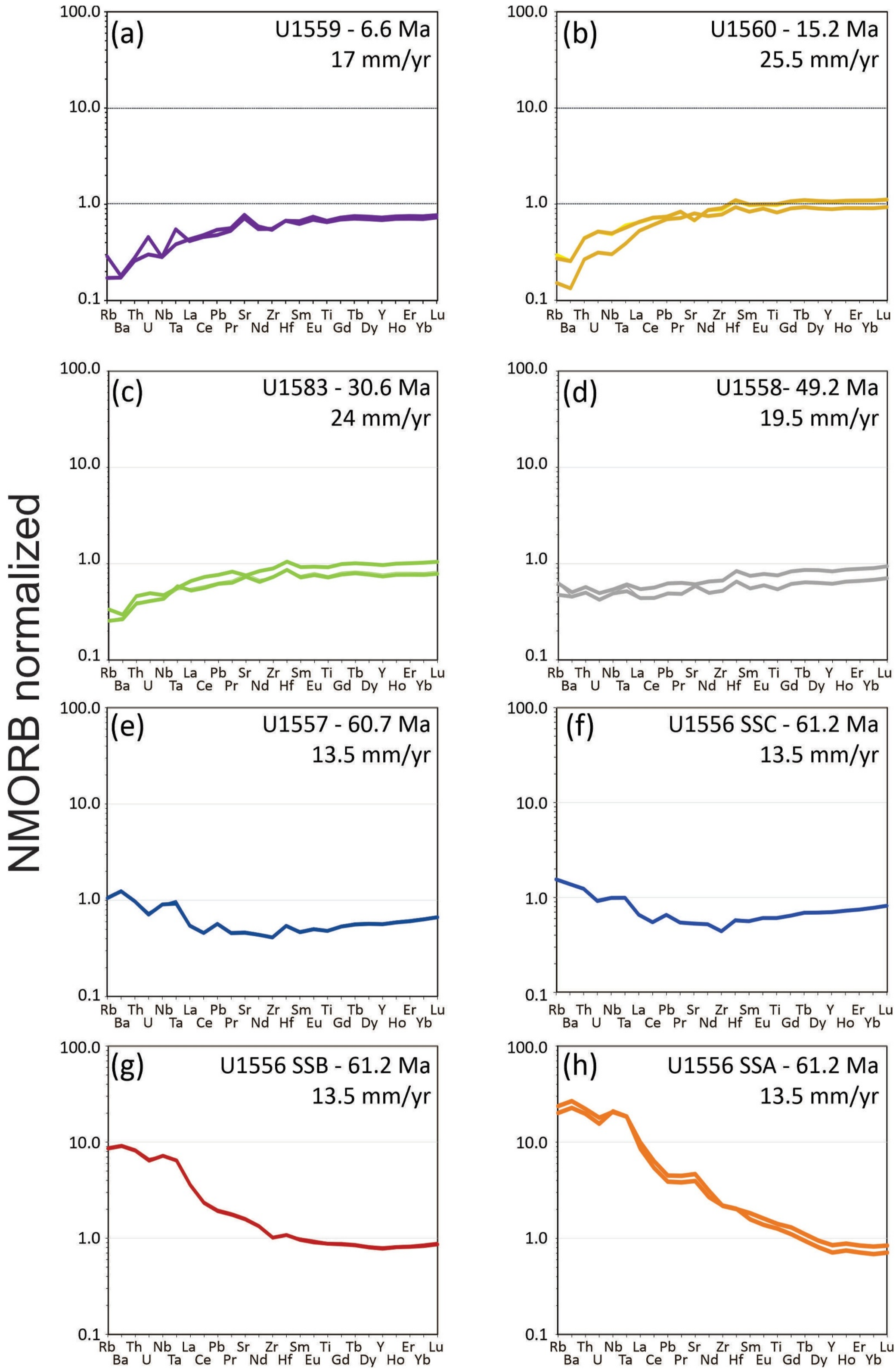

Figure 4. Normalized incompatible trace element diagrams for Sites (a) U1559, (b) U1560, (c) U1583, (d) U1558, (e) U1557, (f) U1556 SSC, (g) U1556 SSB, (h) U1556 SSA. Age and estimated half-spreading rate for each site are shown. Data normalized to the NMORB composition of Gale et al. (2013).

15252027, 2025, 4, Downloaded from https://agupubs.onlinelibrary.wiley.com/doi/10.1029/2025GC012175 by British Geological Survey, Wiley Online Library on [19/05/2025]. See the Terms and Conditions (https://onlinelibrary.wiley.com/terms-and-conditions) on Wiley Online Library for rules of use; OA articles are governed by the applicable Creative Commons License

10.1029/2025GC012175

15252027, 2025, 4, Downloaded from https://agupubs.onlinelibrary.wiley.com/doi/10.1029/2025GC012175 by British Geological Survey, Wiley Online Library on [19/05/2025]. See the Terms and Conditions (https://onlinelibrary.wiley.com/terms-and-conditions) on Wiley Online Library for rules of use; OA articles are governed by the applicable Creative Commons License

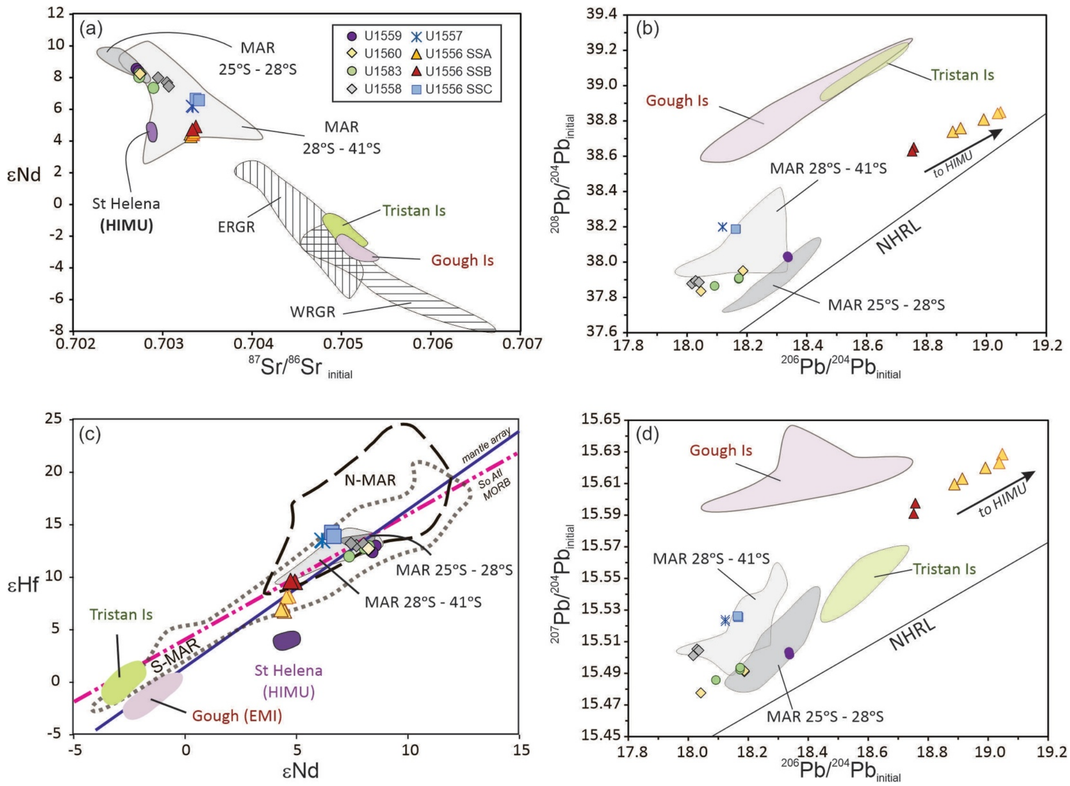

Figure 5. Plots of (a) εNd versus $^{87}Sr/^{86}Sr_{initial}$; (b) $^{208}Pb/^{204}Pb_{initial}$ versus $^{206}Pb/^{204}Pb_{initial}$; (c) εHf versus εNd and (d) $^{207}Pb/^{204}Pb_{initial}$ versus $^{206}Pb/^{204}Pb_{initial}$ for SAT basalts. Mid-Atlantic Ridge (MAR) MORBs 28°–41°S from Class and Lehnert (2012). MAR MORBs 25°–28°S from Regelous et al. (2009) and Li et al. (2023); Pb isotope field excludes one outlier with a high analytical error. Eastern Rio Grande Rise and Western Rio Grande Rise data from Homrighausen et al. (2023). Data for St. Helena, Gough and Tristan da Cunha from Stracke et al. (2022). Northern Hemisphere Reference Line (NHRL) from Hart (1984). Fields for N-MAR (Northern MAR) and S-MAR (Southern MAR) in panel (c) from Agranier et al. (2005). Mantle array (solid blue line) from Chauvel et al. (2008). Regression for the full data set for S-MAR is shown as the pink dot-dash line. Analytical uncertainty within the size of the symbols.

U1556 SSB, have the least depleted isotopic compositions; their εNd values overlap the composition of St Helena, the type locality for high μ OIB (i.e., high time-integrated $^{238}U/^{204}Pb$, HIMU) (Homrighausen, Hoernle, Geldmacher, et al., 2018), although with higher $^{87}Sr/^{86}Sr$. None of the SAT basalts overlap the compositions of Tristan-Gough Islands or the RGR—all of which are derived from sources indicative of far greater time-integrated enrichment, i.e., a source with high Rb/Sr but low Sm/Nd.

Similarly, in Pb-isotope space (Figures 5b and 5d), SAT basalts from sites 30.6 Ma and younger have $^{206}Pb/^{204}Pb$ initial ratios that overlap the field of NMORBs from the ridge axis between 25° and 28°S, although some samples from Sites 1560 and 1583 extend to more depleted (lower) Pb isotope compositions. However, most have higher $^{208}Pb/^{204}Pb$ initial values and plot in a region intermediate between the two MORB fields (Figure 5b). The older tholeiitic basalts from U1558, U1557, and U1556 SSC have similar $^{206}Pb/^{204}Pb$ ratios but even higher $^{208}Pb/^{204}Pb$ (Figure 5b)—and noticeably higher $^{207}Pb/^{204}Pb$ (Figure 5d)—than any of the younger basalts from the transect, plotting within or near the field for plume-influenced MORBs from 28° to 41°S. In contrast, Site U1556 enriched tholeiites (SSB) and alkalic basalts (SSA) have more radiogenic Pb isotope compositions than any other SAT basalts and form well-defined linear arrays in both $^{208}Pb/^{204}Pb$ versus $^{206}Pb/^{204}Pb$ and $^{207}Pb/^{204}Pb$ versus $^{206}Pb/^{204}Pb$ (Figures 5b and 5d). Their high $^{206}Pb/^{204}Pb$ values are distinct not only relative to South Atlantic MORB but also relative to the Tristan and Gough plumes—$^{208}Pb/^{204}Pb$ values are lower for a given $^{206}Pb/^{204}Pb$ than Tristan-Gough whereas their $^{207}Pb/^{204}Pb$ values are intermediate between the two.

There are fewer published Hf isotope data for MORBs in the South Atlantic, particularly for the ridge axis between 25° and 28°S, but the limited data available suggest a similar overlap with the younger SAT basalts, both of which plot on or close to the Nd—Hf mantle array (Figure 5c). Older tholeiites from U1557 and U1556 SSC have lower εNd values but higher εHf than the younger SAT tholeiites and overlap the field for plume-influenced MORBs from 28° to 41°S, plotting above the mantle array. In contrast, the enriched tholeiites, U1556 SSB, and alkalic basalts, U1556 SSA, have both lower εNd and lower εHf. Although they plot within the wider range of MORB compositions from the whole of the South Atlantic (0–54°S), they form a tight linear trend at a high angle to the MORB array, trending toward the composition of St. Helena rather than toward Tristan or Gough Islands.

4. Discussion

4.1. Depleted Mantle Components Sampled by SAT Basalts

Basalts from Sites U1559, U1560, U1583, and to a lesser extent U1558 are unusually depleted in the most incompatible trace elements relative to the mean NMORB composition of Gale et al. (2013) (Figure 4), indicating that these basalts were derived from a source that has undergone greater melt extraction, on average, than NMORB globally. However, their degree of depletion is remarkably similar to that shown by the MORBs from the ridge axis north of SAT (Figure 1)—a region remote from plume influence (25°–28°S) (Li et al., 2023; Regelous et al., 2009). Indeed, normalization of the SAT basalt data to the average composition of basalts from these ridge segments yields relatively flat patterns around a value of one, aside from the most highly incompatible elements (Rb, Ba, and Th), which are slightly to moderately enriched (see Figure S2 in Supporting Information S1).

The Sr, Nd, Pb, and Hf isotope compositions of the younger SAT basalts are also similar to the MORBs between 25° and 28°S (Figure 5). This suggests that SAT basalts from the sites at the eastern end of the transect (≤49.2 Ma) are derived from a mantle source similar to that giving rise to MORBs today between 25° and 28°S—that is, their mantle sources are compositionally similar, underwent similar degrees of partial melting at roughly the same time in Earth history and remained relatively free from subsequent re-enrichment via mantle plumes. A notable difference, however, is the higher $^{208}Pb/^{204}Pb$ for a given $^{206}Pb/^{204}Pb$ of the SAT basalts (Figure 5b), indicating a slightly higher time-integrated Th/U ratio in their mantle source. The higher Th/U ratios are also apparent in the multi-element plots normalized to MORBs from 25° to 28°S (see Figure S2 in Supporting Information S1). This is consistent with a weak DUPAL signature in some of the younger SAT basalts, although considerably smaller than the extreme DUPAL signatures observed further south in the South Atlantic (Class & le Roex, 2011).

In contrast, the concave-upward NMORB-normalized trace element patterns of the older SAT tholeiites (Figures 4e and 4f) indicate a more complicated history that involves at least two stages: a period of melt extraction and depletion followed by re-enrichment of the most highly incompatible elements. As shown by Salters and Stracke (2004), ratios of incompatible elements in basalts that have similar bulk partition coefficients provide a robust indication of these same trace element ratios in the source region, because they are largely unchanged by subsequent magmatic processes. Here, we use the ratio of two highly incompatible trace elements, Th and U, as a proxy for the relative degree of enrichment or depletion in the source (Figure 6) across the 61-million-year timespan of the South Atlantic Transect. For this analysis, we focus on the tholeiitic MORB-like basalts and consider the highly enriched alkali basalts and tholeiites of U1556 SSA and SSB in the next section, although these data are included in Figure 6 for comparison.

Figure 6a shows that Th concentration increases with increasing Th/U, with the youngest SAT tholeiites (U1559) occupying the most depleted (lowest Th and Th/U) end of the array and the oldest tholeiites (U1556 SSC) the least depleted/most enriched end. A positive correlation is also shown for Th/U versus Nb/Y, which indicates that not only is enrichment recorded in the most incompatible trace elements, such as Th/U (Figure 8a), it is also recorded in the overall trace element pattern, since Nb/Y is the ratio of one of the most incompatible elements to one of the least incompatible (Figure 6b). These compositional variations could be interpreted as evidence that the degree of depletion of the mantle source ***increases*** systematically from oldest to youngest across the 61 Myr history of the transect.

However, ratios of HFSE elements from the middle of the incompatible element range (Figure 4), namely plots of Th/U versus Zr/Y and Zr/Ti (Figures 6c and 6d), show a reversal in trend between Sites U1583 (30.6 Ma) and U1558 (49.2 Ma): the trend is broadly positive between U1559 and U1583 (6.6–30.6 Ma) but negative between U1583 and U1556 (30.6–61 Ma). This indicates that the degree of depletion of the mantle source is similar, if not greater, for the older basalts relative to the younger ones, consistent with a re-enrichment event that predominantly affected the most highly incompatible trace element contents of the older SAT basalts (Figures 4e, 4f, 6a,

15252027, 2025, 4, Downloaded from https://agupubs.onlinelibrary.wiley.com/doi/10.1029/2025GC012175 by British Geological Survey, Wiley Online Library on [19/05/2025]. See the Terms and Conditions (https://onlinelibrary.wiley.com/terms-and-conditions) on Wiley Online Library for rules of use; OA articles are governed by the applicable Creative Commons License

15252027, 2025, 4, Downloaded from https://agupubs.onlinelibrary.wiley.com/doi/10.1029/2025GC012175 by British Geological Survey, Wiley Online Library on [19/05/2025]. See the Terms and Conditions (https://onlinelibrary.wiley.com/terms-and-conditions) on Wiley Online Library for rules of use; OA articles are governed by the applicable Creative Commons License

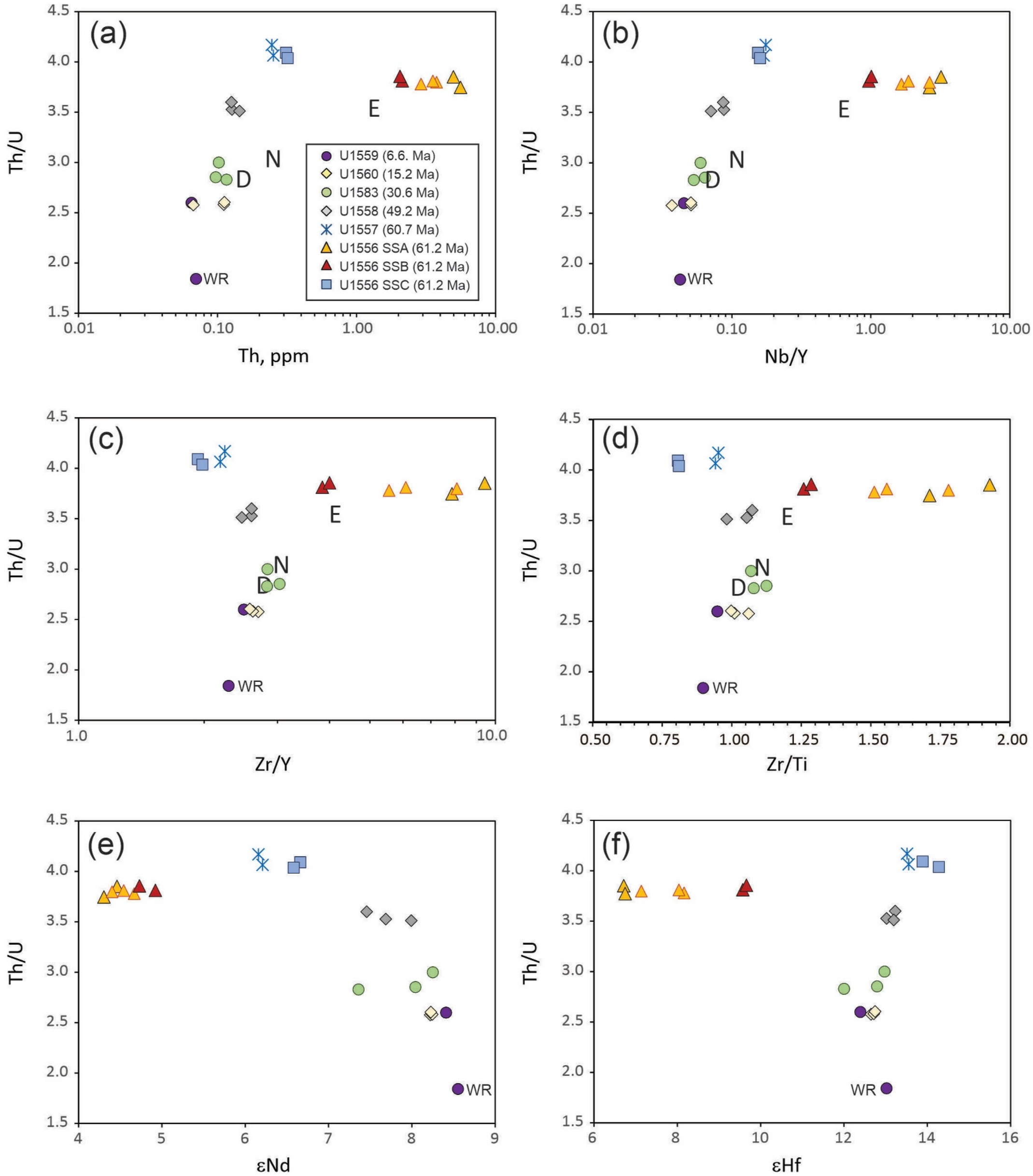

Figure 6. Plots of Th/U versus (a) Th, (b) Nb/Y, (c) Zr/Y, (d) Zr/Ti, (e) εNd, and (f) εHf for SAT basalts. DMORB (D), NMORB (N), and EMORB (E) compositions from Gale et al. (2013) are shown for comparison. Sample labeled WR is the whole rock analysis for U1559-5R-1, 26–30 cm. Although visibly fresh in hand sample, thin section observations show that groundmass mesostasis is partially altered to yellow-brown clay + iron oxyhydroxides (Coggon et al., 2024). Therefore, we cannot rule out the possibility that the lower Th/U ratio has been perturbed by alteration processes. Such limited alteration should have no impact on the Nd and Hf isotopes or HFSE ratios, however.

and 6b). It is also worth noting that the highest Zr/Y and Zr/Ti ratios occur at Sites U1583 and U1560; that is to say, the least depleted mantle source in the transect was sampled between ~15 and 30 Ma when the spreading rates are estimated to have been fastest (24–26 mm/yr; Figure 4).

Re-enrichment of the mantle source is also apparent in the Nd and Hf isotope data (Figures 6e and 6f). In general, Nd and Hf isotopes behave similarly in mantle systems (Jones et al., 2019 and references therein), leading to a strong correlation between the two, creating what is referred to as the Nd—Hf mantle array (Chauvel et al., 2008) (see Figure 5c). However, as shown by Sanfilippo et al. (2021) and Tilhac et al. (2022), Nd and Hf isotopes can be decoupled during melt diffusion and re-enrichment processes, with Nd isotopes being preferentially reset, whereas original Hf ratios are at least partly preserved. This is because the distribution coefficient for Hf is greater than that for Nd during melt—peridotite interactions (i.e., $Kd_{Hf} > Kd_{Nd}$). This can lead to preservation of radiogenic Hf isotope compositions that are inconsistent with the associated Nd isotope ratios, producing compositions that plot well above the Nd-Hf mantle array (see Figure 5c). Such isotope systematics have been interpreted as evidence for ancient melting, which generates high Lu/Hf ratios and radiogenic Hf-isotope compositions over time, followed by recent re-enrichment that reduces the $^{143}Nd/^{144}Nd$ but not the $^{176}Hf/^{177}Hf$ (Tilhac et al., 2022, and references therein). Thus, Nd isotope compositions (and highly incompatible trace-element systematics) tend to reflect the composition of the metasomatizing agent, whereas Hf isotopes are more likely to reflect depletion of the residual protolith.

For SAT basalts, Th/U versus εNd exhibits a concave downward distribution with an overall negative slope (Figure 6e)—both parameters suggest that the youngest basalts record the greatest source depletion (low Th/U and high εNd), whereas the oldest basalts record the greatest enrichment or least depletion (high Th/U and low εNd), in common with Th/U versus Nb/Y (Figure 6b). In contrast, a plot of Th/U versus εHf shows a broadly positive slope in which the most depleted mantle source is that sampled by the oldest SAT basalts from Sites U1557 and U1556 SSC. Basalts from sites 30.6 Ma and younger show some variability in εHf but are, in general, derived from a less depleted source, with 49.2 Ma Site U1558 basalts being intermediate between the two groups.

In summary, since at least 49.2 Ma, the MAR at ~31°S has tapped a mantle source that is similar to that of MORBs currently erupting between 25° and 28°S. That source is more depleted than the NMORB composition of Gale et al. (2013) and more similar to their mean DMORB, particularly for Site U1558 (see Figure S3 in Supporting Information S1). In contrast, Nd-Hf-isotopes, combined with trace element systematics, lead us to conclude that the older SAT tholeiites from U1557 and U1556 SSC were derived from a mantle source that experienced greater (time-integrated) depletion but was subsequently re-enriched more recently in the most highly incompatible trace elements (Figures 4 and 6). The higher Th/U, Nb/Y, and lower εNd of Site U1558 basalts relative to the younger SAT basalts suggest that the effects of re-enrichment can be observed until at least 49.2 Ma.

4.1.1. Nature of Enriched Components—HIMU Beneath the South American Plate

The basement stratigraphy recovered from the oldest SAT site (U1556; 61.2 Ma) is more complex than that from the younger sites, with MORB-like basalts at the bottom of Hole U1556C (Stratigraphic Sequence C, SSC) but OIB-like basalts at the top (Stratigraphic Sequence A, SSA). The intervening stratigraphic sequence (SSB) consists of (re)enriched tholeiitic basalts that have trace element characteristics intermediate between SSA and SSC (Figures 4f–4h). The U1556 basalts, along with basalt clasts from the talus breccias at Site U1557 (60.7 Ma), are also isotopically distinct from younger MORBs along the transect (Figure 5). They have higher $^{87}Sr/^{86}Sr_i$ and lower εNd, with U1556 SSA and SSB occupying the lower εNd end of a near-vertical array in εNd versus initial $^{87}Sr/^{86}Sr$ (Figure 5a). Pb isotope ratios are variable and characterized by higher $^{207}Pb/^{204}Pb_i$ and $^{208}Pb/^{204}Pb_i$ for a given $^{206}Pb/^{204}Pb_i$ (Figures 5b and 5d). The compositions of U1556 SSA alkali basalts and SSB enriched tholeiites are particularly notable, because they are distinct not only relative to younger SAT basalts but also relative to the Tristan—Gough plume system. Instead, their high $^{206}Pb/^{204}Pb_i$ ratios indicate the presence of a HIMU plume component in the mantle source (Figures 5b and 5d) rather than Enriched Mantle I (EMI) like Tristan-Gough. This is surprising because St. Helena, the type locality for HIMU, is located ~2,500 km north of the SAT (Figure 1).

Consistent with the presence of a HIMU component in these basalts, however, is the tight linear array that trends toward the composition of St. Helena in εHf versus εNd (Figure 5c). This array has a high correlation coefficient ($R^2 = 0.85$, $n = 7$) and a steeper slope than that of the Nd—Hf mantle array (Chauvel et al., 2008) or the array created by the field for all South Atlantic MORBs (0–54°S) (Figure 5c). Although the central South Atlantic has been dominated by EMI-type plume systems (Class et al., 2023; Homrighausen et al., 2019, 2023; Rohde et al., 2013), the presence of a HIMU component has been reported in some off-axis seamounts that occur adjacent to the Walvis Ridge (Homrighausen et al., 2019) and along the nearby Namibian coast (Zhou et al., 2022). In Pb isotope space, these samples form an array with a similar slope to that produced by U1556 SSA and SSB, but it extends to even more radiogenic $^{206}Pb/^{204}Pb_i$, reaching values almost as radiogenic as those of St. Helena (Figures 7a and 7c). These seamounts range in age from ~77 Ma near the Namibian coast to ~53 Ma at the southwestern end of Valdivia Bank (Figure 1) (Homrighausen et al., 2019) and, as such, they overlap in age with

15252027, 2025, 4, Downloaded from https://agupubs.onlinelibrary.wiley.com/doi/10.1029/2025GC012175 by British Geological Survey, Wiley Online Library on [19/05/2025]. See the Terms and Conditions (https://onlinelibrary.wiley.com/terms-and-conditions) on Wiley Online Library for rules of use; OA articles are governed by the applicable Creative Commons License

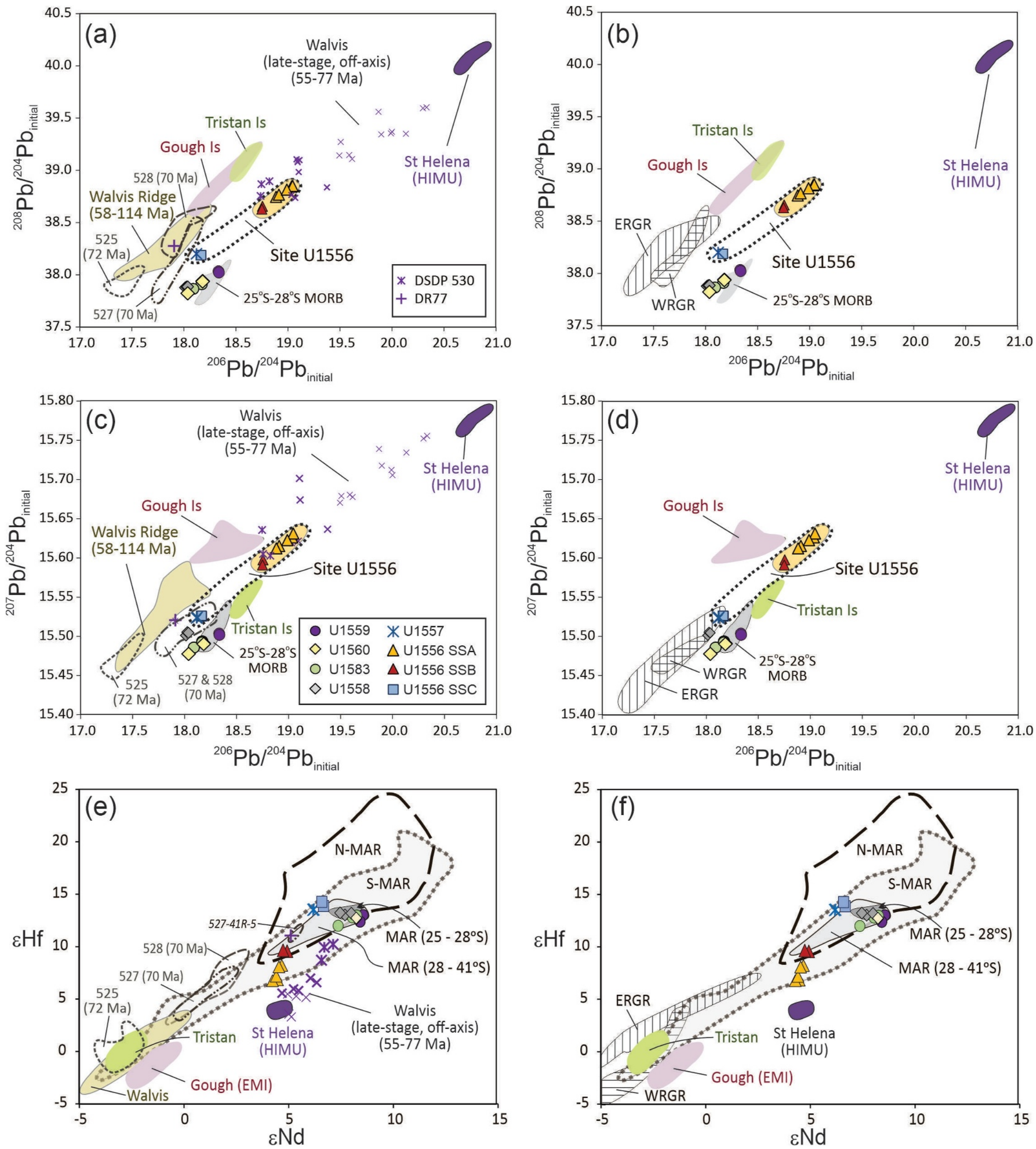

Figure 7. Plots of (a, b) $^{208}Pb/^{204}Pb_{initial}$ versus $^{206}Pb/^{204}Pb_{initial}$, (c, d) $^{207}Pb/^{204}Pb_{initial}$ versus $^{206}Pb/^{204}Pb_{initial}$ and (e, f) εHf versus εNd for SAT basalts. Panels a, c, and e compare the SAT data to Walvis Ridge, DSDP sites 525, 527, 528, and 530, and DR77. Late-stage, off-axis HIMU magmatism from the Walvis Ridge is shown as purple crosses; HIMU Walvis samples from "ridge-like seamounts" denoted by crosses with thicker line width. Panels b, d, and f compare the SAT data to Eastern and Western RGR (ERGR and WRGR). Fields for ERGR, WRGR, DSDP 525, 527, 528, and Walvis Ridge from Homrighausen et al. (2023); field for WRGR excludes one sample with high $^{206}Pb/^{204}Pb$, which also has unusually low SiO_2 contents, suggesting alteration. Data for late-stage, off-axis HIMU, DSDP 530, and DR77 from Homrighausen, Hoernle, Geldmacher, et al. (2018). Data for St. Helena, Gough, and Tristan da Cunha Islands from Stracke et al. (2022). Mid-Atlantic Ridge (MAR) MORBs 25°–28°S from Regelous et al. (2009) and Li et al. (2023); Pb isotope field excludes one outlier with a high analytical error. Fields for N-MAR (Northern MAR) and S-MAR (Southern MAR) (panels e and f) from Agranier et al. (2005); MAR MORBs 28°–41°S from Class and Lehnert (2012).

the 61 Ma basalts from Sites U1556 and U1557. However, they are 20–40 Myr younger than the underlying or adjacent Walvis Ridge basement. Homrighausen, Hoernle, Geldmacher, et al. (2018) interpret this volcanism as the product of a late-stage, off-axis HIMU-event superimposed upon the older (EMI—type) Walvis Ridge. Although the Tristan-Gough EMI-type plumes are thought to have ascended from the margins of the Large Low Shear Velocity Province (LLSVP) present beneath the region (Burke et al., 2008; French & Romanowicz, 2015; Homrighausen et al., 2019; Torsvik et al., 2006), the HIMU-type plume (or multiple small "plumelets") is inferred

15252027, 2025, 4, Downloaded from https://agupubs.onlinelibrary.wiley.com/doi/10.1029/2025GC012175 by British Geological Survey, Wiley Online Library on [19/05/2025]. See the Terms and Conditions (https://onlinelibrary.wiley.com/terms-and-conditions) on Wiley Online Library for rules of use; OA articles are governed by the applicable Creative Commons License

10.1029/2025GC012175

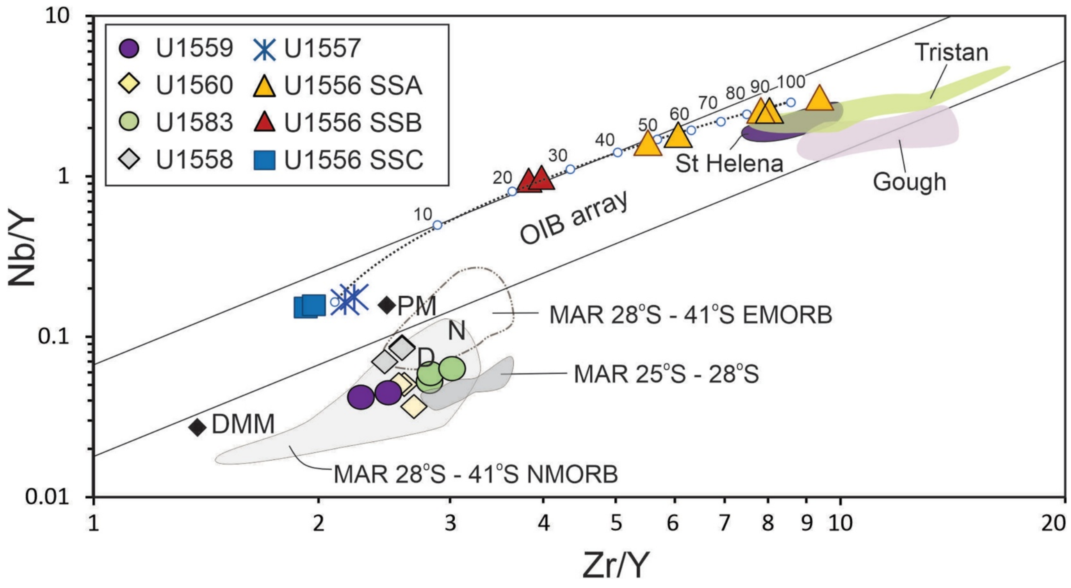

Figure 8. Plot of Nb/Y versus Zr/Y for SAT basalts. Position of "tramlines" that define the OIB array from Fitton et al. (1997). Mixing calculations assume average concentrations (in ppm) of Nb = 75, Y = 26, Zr = 222.5 for U1556 SSA and Nb = 3.5, Y = 21, Zr = 44 for U1556 SSC. Mid-Atlantic Ridge (MAR) MORBs 25°–28°S from Regelous et al. (2009) and Li et al. (2023). MAR MORBs 28°–41°S from Class and Lehnert (2012) and EarthChem. MAR MORB 28°–41°S data set filtered to distinguish NMORB (light gray field) from EMORB (dot-dash line) on the basis of chondrite-normalized La/Sm < 0.63 (Schilling, 1973). Fields for St. Helena, Tristan, and Gough from Willbold and Stracke (2006). PM (primitive mantle) from Sun and McDonough (1989). DMM (depleted MORB mantle) from Workman and Hart (2005). N denotes the average NMORB composition from Gale et al. (2013).

to have ascended from the interior of the LLSVP beneath the continent of Africa (Homrighausen et al., 2020; Zhou et al., 2022). Upon reaching the lithosphere-asthenosphere boundary beneath Africa, the plume(s) were deflected toward the region of thinner oceanic lithosphere via a process called "upside-down drainage" (Gassmöller et al., 2016; Sleep, 1997).

While this occurrence establishes the presence of a HIMU-like component within the same general region of the South Atlantic as SAT, its influence on the African plate does not appear to extend beyond Valdivia Bank (Homrighausen, Hoernle, Geldmacher, et al., 2018), let alone to the South American Plate. Moreover, there is no evidence that the SAT basalts at Site U1556 (or Site U1557) represent a late-stage event relative to the ~93–68 Ma ERGR (O'Connor & Jokat, 2015; Rohde et al., 2013). Mixing between ERGR and MORB or ERGR and Tristan-Gough would not produce the Pb isotope compositions of U1556 SSA or SSB (Figures 7b and 7d), nor is there evidence that the U1556 basalts are anomalously young. Rather, the middle Paleocene assemblage of planktic foraminifera of U1556 and U1557 basal sediments are consistent with the predicted ~61 Ma crustal age, and planktic foraminifera preserved in a thin interflow sediment from the deepest core in Hole U1556B indicate that the entire 341 m basalt sequence cored erupted within 220 kyr (Coggon et al., 2024).

Our new isotope results thus provide the first evidence for a HIMU component beneath the South American plate in a region where the plume component was previously inferred to be entirely from the EMI-type Tristan-Gough plume system (Class et al., 2023; Homrighausen et al., 2019, 2023). Indeed, although a HIMU component has been recognized on the Namibian and South African coasts, such a signal is missing in late-stage post-Paraná alkaline magmatism (Gibson et al., 2005). The question is, how did this component make its way to this part of the South Atlantic beneath the South American plate?

In the next section, we propose a geodynamic model to explain the presence of this HIMU component, but first we must establish the nature of the mantle source for the temporally and spatially associated tholeiitic basalts at the bottom of Hole 1556B (i.e., SSC) and from Site U1557. As shown in Figures 5 and 7, these basalts are isotopically distinct relative to the younger SAT tholeiites (<49.2 Ma) as well as to the contemporaneous basalts of U1556 SSA and SSB. But is their mantle source part of the shallow convecting asthenosphere (MORB-source mantle) or are they associated with the HIMU-like plume source of U1556 SSA and SSB? We consider three alternatives: (a)

15252027, 2025, 4, Downloaded from https://agupubs.onlinelibrary.wiley.com/doi/10.1029/2025GC012175 by British Geological Survey, Wiley Online Library on [19/05/2025]. See the Terms and Conditions (https://onlinelibrary.wiley.com/terms-and-conditions) on Wiley Online Library for rules of use; OA articles are governed by the applicable Creative Commons License

10.1029/2025GC012175

partial melting of pre-existing shallow asthenosphere or MORB-source mantle, (b) contamination of MORB-source mantle by the Tristan-Gough EMI-type plume system during formation of the ERGR, that is, interaction between deep and shallow mantle, and (c) derivation from a depleted component associated with the HIMU plume that produced the U1556 SSA alkali basalts; hence, delivered to the shallow, convecting asthenosphere from the lower mantle.

Distinguishing among these scenarios has significant implications for the geodynamic evolution of the South Atlantic and the role of mantle plumes in the generation of MORB-source mantle. Indeed, recent analysis of isotopic data for oceanic basalts using machine learning (Stracke et al., 2022) has led to the suggestion that "…the actively upwelling mantle under most OIB locations may contain a greater proportion and/or more incompatible element depleted, residual mantle than the sub-ridge mantle"—a proposal contrary to most models for the source of OIBs but that supports the growing consensus that asthenospheric mantle, "polluted by mantle plumes," is more depleted, on average, than previously thought (Sani et al., 2023; Stracke et al., 2019; Tucker et al., 2020; Willbold & Stracke, 2006).

The first scenario, which involves partial melting of MORB-source mantle, can be ruled out based on the high $^{207}Pb/^{204}Pb_i$ and $^{208}Pb/^{204}Pb_i$ ratios for a given $^{206}Pb/^{204}Pb_i$ of the U1556 SSC and U1557 basalts, which are distinct from the composition of normal depleted MORB-source mantle (Figures 5b, 5d, 7a, and 7c). However, the data do not immediately rule out scenario (ii), that is, contamination of the depleted MORB source by an enriched plume component, such as Tristan-Gough. Sr—Nd and Pb—Pb isotope systematics are ambiguous in this regard. Pb-isotope systematics, for example, are consistent with mixing between the Gough plume component and a depleted mantle similar to that supplying the basalts at Sites U1560 and U1583 (since mixing in Pb-Pb isotope space produces a straight line) (Figures 7a and 7c). Note, however, that the high $^{206}Pb/^{204}Pb_i$ and relatively low $^{207}Pb/^{204}Pb_i$ values of the Tristan plume rule it out as the contaminant in this scenario (Figure 7c). Similarly, U1556 SSC and U1557 tholeiitic basalts overlap the composition of the ERGR—which is believed to have formed by plume-ridge interaction involving the Triston-Gough plume system (Class et al., 2023; Homrighausen et al., 2023; Rohde et al., 2013)—in $^{207}Pb/^{204}Pb_i$ versus $^{206}Pb/^{204}Pb_i$ (Figure 7d), although they are compositionally distinct from it in $^{208}Pb/^{204}Pb_i$ versus $^{206}Pb/^{204}Pb_i$ (Figure 7b).

However, scenario (ii) is ruled out by Nd-Hf isotope systematics (Figures 7e and 7f). Although U1556 SSC and U1557 basalts plot within the field for ***all*** South Atlantic MORBs (0–54°S), they plot outside the field for South Atlantic MORBs between 28° and 41°S, the region where there is evidence that the MORB-source mantle has been polluted by the Tristan- Gough plume (Andres et al., 2004; Class & le Roex, 2011; Fontignie & Schilling, 1996; Gassmöller et al., 2016)—specifically, these basalts have higher εHf values for a given εNd (Figures 7e and 7f). Mixing between the Gough plume and MORB-source mantle, like that tapped by the younger SAT sites or MORBs between 25° and 28°S, cannot produce these higher εHf values; instead, such mixing produces an elongate array that parallels the mantle array, as shown by MORBs from 28° to 41°S (Figures 7e and 7f). To generate the higher εHf values of U1556 SSC and U1557 through contamination by the Gough plume, the starting depleted mantle composition would have to have higher εHf and εNd than any source currently observed in the region (see mixing calculations, Figure S3 in Supporting Information S1). Although suitably depleted isotopic compositions exist in some locations in the South Atlantic (Figures 7e and 7f), they have currently only been sampled from ridge segments north of ~14°S and south of ~44°S—the former attributed to interactions with the Sierra Leone plume system and the latter with the Discovery—Shona plume system (Agranier et al., 2005; Andres et al., 2004).

Therefore, the most likely explanation is that U1556 SSC and U1557 basalts were derived from a depleted component associated with the HIMU-like plume that gave rise to U1556 SSA and SSB. Although not conclusive, the fact that their compositions plot at the depleted end of the linear array in Pb-isotope space produced by the more radiogenic samples from Site U1556 (Figure 7a) is consistent with this interpretation. Similarly, they can be modeled as the depleted end member of a mixing array in εHf versus εNd that includes the same plume-related basalts of U1556 SSA and SSB (Figure S3 in Supporting Information S1). In addition, in a plot of $\Delta84$ versus εHf, where $\Delta 8/4 = (^{208}Pb/^{204}Pb_{sample} - ^{208}Pb/^{204}Pb_{NHRL}) \times 100$ (Hart, 1984), U1557 and U1556 SSC basalts have higher εHf values that preclude mixing between Tristan—Gough and MORB-source mantle; that is, Gough and Tristan, as well as Walvis Ridge and the ERGR, have significantly lower εHf and higher $\Delta84$, whereas MORBs between 25°and 28°S have both lower εHf and $\Delta84$ (see Figure S4 in Supporting Information S1).

15252027, 2025, 4, Downloaded from https://agupubs.onlinelibrary.wiley.com/doi/10.1029/2025GC012175 by British Geological Survey, Wiley Online Library on [19/05/2025]. See the Terms and Conditions (https://onlinelibrary.wiley.com/terms-and-conditions) on Wiley Online Library for rules of use; OA articles are governed by the applicable Creative Commons License

15252027, 2025, 4, Downloaded from https://agupubs.onlinelibrary.wiley.com/doi/10.1029/2025GC012175 by British Geological Survey, Wiley Online Library on [19/05/2025]. See the Terms and Conditions (https://onlinelibrary.wiley.com/terms-and-conditions) on Wiley Online Library for rules of use; OA articles are governed by the applicable Creative Commons License

Further support for this interpretation comes from the distribution of data in the Nb/Y versus Zr/Y discrimination diagram (Figure 8). Although this diagram was originally developed for the study of Iceland and the associated Reykjanes Ridge (Fitton et al., 1997), it has proven to be useful for discrimination of MORB and OIB mantle sources and the study of ocean island basalts more generally, for example, Louisville seamounts (Vanderkluysen et al., 2014), Hawaii (Garcia et al., 2016; Harrison et al., 2020), Kerguelen (Doucet et al., 2002) and Galapagos (Harpp & Weis, 2020). Because Zr and Nb behave similarly relative to Y during mantle melting, variations in the degree of partial melting produce arrays parallel to the "tramlines" shown in Figure 8. Variations in source composition determine whether the samples plot above or below the lower tramline. Ocean island basalts tend to plot in the region between the two "tramlines," whereas MORBs plot below the lower tramline, with Zr/Y ratios toward the lower end of the range. Therefore, plotting above the lower tramline has been interpreted as evidence of a lower mantle origin (OIB field), whereas plotting below the lower tramline corresponds to derivation from a depleted MORB-source mantle.

Figure 8 shows that U1556 SSA and SSB plot within the OIB field and the most OIB-like basalts from the top of U1556 SSA overlap the compositions of St. Helena and Tristan da Cunha plume magmatism. All SAT basalts younger than 49.2 Ma plot below the lower tramline and overlap the field for MORBs between 25° and 41°S. In contrast, U1556 SSC and U1557 basalts plot within the tramlines, having similar Zr/Y ratios to MORB but higher Nb/Y. Moreover, all the 61-Ma SAT basalts can be modeled on this diagram as the product of mixing between U1556 SSC tholeiites and the alkali basalts of U1556 SSA, consistent with the data distribution in Sr-Nd-Pb-Hf isotope space (Figure 5 and Figure S3 in Supporting Information S1). In contrast, Gough Island basalts tend to have lower Nb/Y for a given Zr/Y than Tristan da Cunha, St. Helena and U1556 SSA basalts, which further excludes mixing between Gough and depleted mantle as an explanation for U1556 SSC and U1557 tholeiites. A companion version of Figure 8 is provided in Figure S5 in Supporting Information S1 that includes data for Walvis Ridge, DR77, DSDP Sites 525, 527, 528, and 530, and the late-stage, off-axis HIMU samples. The figure highlights the distinctive compositions of U1556 SSC and U1557 tholeiites relative to these other localities.

We therefore conclude that U1556 SSC and U1557 basalts represent a depleted component associated with the HIMU plume that gave rise to SSA and SSB. As shown in Figures 4 and 6, that component was re-enriched prior to melt generation, and we propose a geodynamic model to explain this, as well as the presence of HIMU in this region of the South Atlantic, in the next section.

4.1.2. Geodynamic Model for the Origin of SAT Basalts

The presence of a HIMU component in SAT basalts is unexpected because St. Helena is more than 2,500 km to the NE (Figure 1). Moreover, the direction of upper mantle flow in the region is predicted to be to the west (Colli et al., 2014), so significant transfer of HIMU material through the upper mantle from the northeast seems unlikely. Alternatively, it has been suggested that large plume heads that ascend beneath continents can spread out for thousands of kilometers prior to continental breakup (Douglass & Schilling, 2000; Fontignie & Schilling, 1996). However, if such a major HIMU plume event had occurred prior to the breakup of Gondwana, the consequences would have been widespread, whereas the HIMU component in this part of the south Atlantic appears to be localized and of relatively small volume. Indeed, the crustal thickness at Sites U1556 and U1557 is anomalously thin (∼3.6 km), which is interpreted as evidence for an underlying mantle that is either colder or more depleted than normal (Christeson et al., 2020), inconsistent with volcanism associated with a large plume head. In addition, the relatively flat HREE patterns for even the most enriched SAT basalts (Figure 4) indicate the last equilibration of their parental melts within the spinel lherzolite field; that is, melt generation occurred at relatively shallow depths, such as beneath spreading ridges, rather than in upwelling plumes.

TiO_2/Yb versus Nb/Yb systematics are consistent with this interpretation (Figure 9). In this diagram, variations in the TiO_2/Yb ratio of mantle-derived basalts are largely controlled by the pressure of melting, whereas Nb/Yb ratios reflect the degree of melting and/or degree of source enrichment (Pearce, 2008). Although U1556 SSA basalts from above the mixed interval in Hole U1556B (see Figure 2) plot within the alkaline OIB field, their relatively low TiO_2/Yb values plot below the fields for St. Helena and Tristan-Gough near the boundary with the EMORB field, indicating pressures of melting that were ≤3 GPa, that is, <∼90 km (Figure 9). Collectively, the U1556 SSA and SSB basalt data form a linear array that extends from the alkaline OIB field to the field for tholeiitic EMORBs, a distribution indicative of plume-ridge interaction on this diagram (Pearce, 2008) and in line with the geochemical evidence for mixing presented earlier (Figures 3, 5, and 8). However, the array is offset to

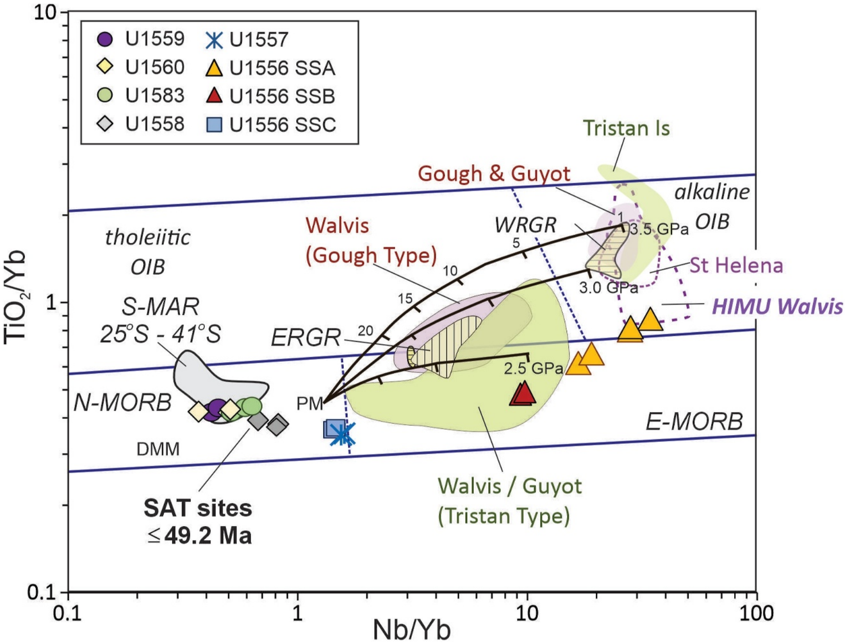

Figure 9. TiO_2/Yb versus Nb/Yb discrimination diagram for SAT basalts. Discrimination boundaries and melting curves from Pearce (2008). Mid-Atlantic Ridge MORBs 25°–41°S from Regelous et al. (2009), Li et al. (2023) and Class and Lehnert (2012). Fields for St. Helena, Tristan, and Gough from Willbold and Stracke (2006). Field for Walvis late-stage, off-axis HIMU rocks (Homrighausen, Hoernle, Geldmacher, et al., 2018) outlined by the black dashed line. Eastern Rio Grande Rise, Western Rio Grande Rise, Walvis Ridge, and Tristan-Gough Guyot Province data from Homrighausen et al. (2023); data plotted excludes evolved samples with MgO <5 wt% to minimize the effects of fractional crystallization processes on the TiO_2/Y ratio. This ratio is largely unaffected by fractional crystallization in basalts, but it can be affected by fractionation of Ti-rich phases, such as ilmenite, in more evolved rocks (Pearce, 2008). PM (primitive mantle) from Sun and McDonough. DMM (depleted MORB mantle) from Workman and Hart (2005).

higher Nb/Yb values than expected for even 1% partial melting of primitive mantle, which suggests either very low degrees of partial melting (<<1%) or, more likely (given the major element compositions; Figure 3), derivation from a mantle source more enriched than primitive mantle (Pearce, 2008). The latter interpretation is consistent with the enrichment, or re-enrichment, shown by ≥49 Ma SAT basalts in multi-element plots (Figures 4e–4h).

By comparison, Walvis late-stage, off-axis HIMU magmatism forms a near-vertical array that spreads between values for Tristan da Cunha and St. Helena and those of the most enriched U1556 SSA basalts (Figure 9). The HIMU Walvis samples with the lowest TiO_2/Yb ratios were recovered from "ridge-like seamounts" located west of Valdivia Bank (dredge sites DR45 and DR46); these are also the youngest (53–54 Ma) HIMU samples reported by Homrighausen, Hoernle, Geldmacher, et al. (2018). Slightly older ridge-like seamounts were also sampled on the western side of Valdivia Bank from a site further north, DR75 (~63 Ma). Although these samples are too evolved to be plotted on the TiO_2/Yb versus Nb/Yb discrimination diagram (see Pearce, 2008, for explanation), in combination with DR45 and DR46, they suggest an association between style of emplacement, depth of melting, and composition. In particular, the ridge-like seamount samples have the lowest $^{206}Pb/^{204}Pb_i$ values (<19.4) and highest εHf (>5.5) of the Walvis HIMU rocks, that is, they are the least HIMU like. These compositions also overlap with those of U1556 SSA basalts (Figures 7a, 7c, and 9). In contrast, the Walvis HIMU samples with the most radiogenic Pb isotope ratios, those that are most HIMU-like, tend to be older (>~65 Ma) and occur as either isolated seamounts or discrete edifices superimposed on the older sections of the Walvis Ridge, nearer to the African coast. Their higher TiO_2/Yb ratios, which overlap the composition of St. Helena (Figure 9), indicate derivation by partial melting at higher pressures (>3 GPa) than the magmatism at ridge-like seamounts. These observations suggest that not only did the HIMU magmatic event progress to the south and west along the Walvis ridge over time (Homrighausen et al., 2020) but also that the HIMU character is linked in some way to the depth of melting, which we discuss in the model below.

15252027, 2025, 4, Downloaded from https://agupubs.onlinelibrary.wiley.com/doi/10.1029/2025GC012175 by British Geological Survey, Wiley Online Library on [19/05/2025]. See the Terms and Conditions (https://onlinelibrary.wiley.com/terms-and-conditions) on Wiley Online Library for rules of use; OA articles are governed by the applicable Creative Commons License

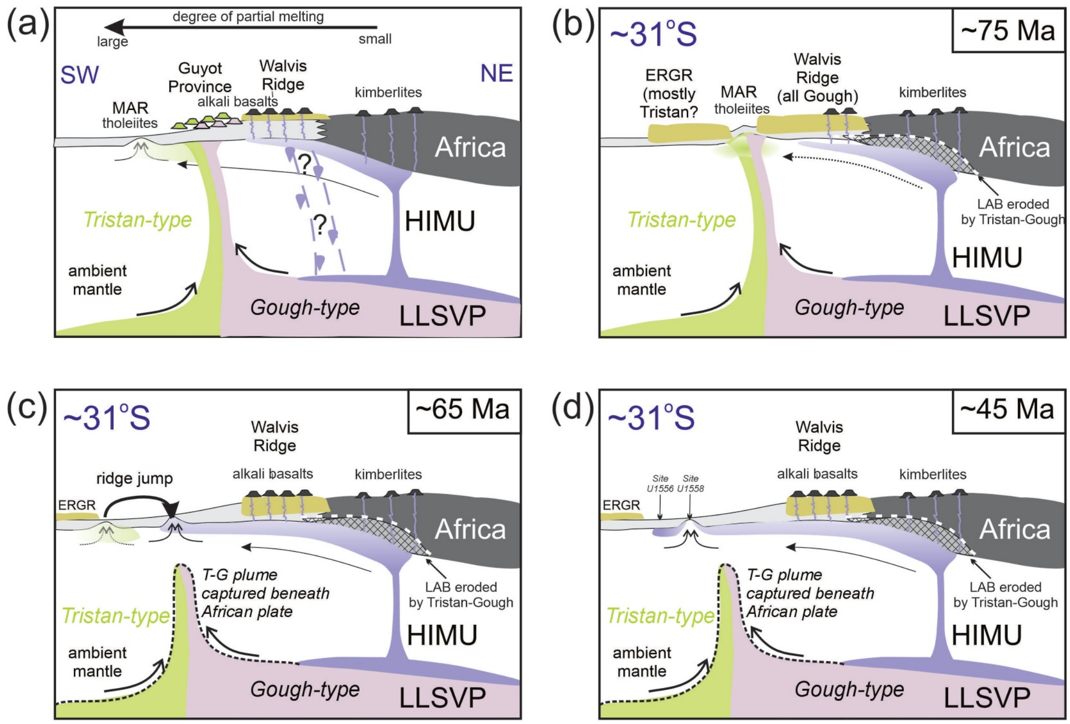

Figure 10. (a) Schematic model (not to scale) modified from Homrighausen, Hoernle, Geldmacher, et al. (2018) showing the origin of late Cretaceous—Paleogene HIMU-type volcanism along the Walvis hotspot track and adjacent African continent. The orientation of this cross-section is roughly NE—SW along the axis of the Walvis ridge. The Tristan-Gough EMI-type plume, a source of Walvis Ridge magmatism, is shown ascending from the margins of the African LLSVP. The source of Walvis late-stage, off-axis HIMU magmatism is shown as either an individual upwelling plume or as clusters of smaller "plumelets," both of which originate from a layer overlying the EMI layer but from a region interior to the LLSVP rather than along its margins. Thinning of the lithosphere from the African continent toward the South Atlantic Ocean deflects the plume (s) westward beneath the Walvis Ridge. Note that for this projection and time (ca. 65 Ma; Homrighausen, Hoernle, Geldmacher, et al., 2018) the Tristan-Gough plume is not ridge centered. (b) Cartoon showing the geodynamic scenario envisaged for the region at ~31°S, prior to SAT (~75 Ma). At this latitude, the Tristan-Gough plume is ridge-centered, producing the RGR. Late-stage HIMU plume magmatism begins along the Walvis ridge near the African continent. The white dashed line reflects the paleo lithosphere-asthenosphere boundary after thinning of the lithosphere in response to continental breakup and arrival of the EMI-type Tristan-Gough plume (Pandey et al., 2022). The crosshatched region represents the re-thickening of the lithosphere in response to subsequent magmatic processes. (c) By ~65 Ma, the EMI-type Tristan-Gough plume is stranded further south beneath the African plate, not beneath the ridge. To distinguish this from the ascent that reaches the surface at the latitude of the Eastern Rio Grande Rise (and SAT), as per panel (b), the ascending plume is shown here outlined by a dashed line. One or more ridge jumps relocate the spreading center eastward at ~31°S so that spreading now takes place over the remnants of the HIMU plume that gave rise to the late-stage magmatism along the Walvis Ridge. (d) By 45 Ma, spreading at the ridge axis has largely replaced the HIMU plume material with a more typical MORB-source mantle. Basalts from Site U1558 record the transition back to the NMORB source mantle.

In contrast, SAT basalts from sites 49.2 Ma and younger plot within the NMORB field and overlap the compositions of NMORBs from the current ridge axis between 25° and 41°S. U1556 SSC and U1557 tholeiites are compositionally distinct from the younger tholeiites, plotting on the boundary between NMORB and EMORB, consistent with their derivation from a depleted mantle that was subsequently re-enriched in the most incompatible trace elements (Figures 4e and 4f).

When considered collectively, these observations require that any geodynamic model for the origin of SAT basalts explains not only the presence of a HIMU component on the South America plate adjacent to the ERGR but also the generation of OIB-like magmas at lower pressures than is typical of most OIBs, along with the creation of anomalously thin crust from a mantle that is either unusually depleted or unusually cold (Christeson et al., 2020).

Homrighausen, Hoernle, Geldmacher, et al. (2018) proposed two different mechanisms to explain the presence of a HIMU component in the late-stage-off-axis Walvis volcanism (Figure 10a): (a) a single plume that impinged

15252027, 2025, 4, Downloaded from https://agupubs.onlinelibrary.wiley.com/doi/10.1029/2025GC012175 by British Geological Survey, Wiley Online Library on [19/05/2025]. See the Terms and Conditions (https://onlinelibrary.wiley.com/terms-and-conditions) on Wiley Online Library for rules of use; OA articles are governed by the applicable Creative Commons License

10.1029/2025GC012175

upon the base of the African lithosphere and was deflected toward the thinner oceanic lithosphere ("upside down drainage"), or (b) clusters of much smaller "plumelets" that ascended variously beneath the African continent and the oceanic crust. As explained below, and consistent with Homrighausen et al. (2020) and Zhou et al. (2022), we find that a single plume better explains the full range of observations, including both the presence of a HIMU component in Sites U1556 and U1557 basalts and the unusual magmatic stratigraphy observed at Site U1556.

Between 93 and 83 Ma, the Tristan-Gough plume (predominantly Gough at this time) was centered beneath a long, oblique, SW-NE-trending segment of the MAR (O'Connor & Jokat, 2015) (Figure 11; also see Figure 15 of Sager et al. (2021) for an excellent representation of the bathymetry and tectonic changes in the South Atlantic during the late Cretaceous and early Paleogene). The plume tail and African plate were migrating eastward but at roughly the same rate, so their positions relative to one another remained the same (Gassmöller et al., 2016). As a result, the plume remained close to the ridge, leading to high melt production and formation of Valdivia Bank and the RGR (Figure 10a). Interaction between the MAR and the Tristan-Gough plume continued from ~83 to 72 Ma, but the spreading axis adopted a more N-S orientation (Gassmöller et al., 2016; Sager et al., 2021). This initially produced smaller, ridge-parallel edifices west of Valdivia Bank and generated the ERGR (Figures 10b and 11b). The HIMU event begins along the Walvis Ridge during this interval, by ~77 Ma, forming the late-stage off-axis seamounts along the older portions of the ridge near the Namibian coast (Homrighausen, Hoernle, Geldmacher, et al., 2018). Some South African Group I kimberlites and carbonatites of Namibia are also believed to be associated with this HIMU plume event (Homrighausen, Hoernle, Hauff, et al., 2018, 2019; Zhou et al., 2022), potentially pushing plume arrival beneath the African continent back to ~120 Ma. Why the HIMU plume ended up focused beneath the Walvis Ridge is unknown, but we note that the lithosphere here was significantly thinned to ~80 km at the time of continental breakup (Pandey et al., 2022), which was presumably facilitated, if not caused, by the earlier Tristan-Gough plume. The lithosphere in the region has gradually re-thickened through magmatic processes (Pandey et al., 2022), but the thinner lithosphere in the region at the time of the HIMU plume may have funneled it toward the ridge as part of an "upside down drainage" process (Figures 10a and 10b).

Between ~70 and 60 Ma, the ridge migrated away from the Tristan-Gough plume tail, stranding it beneath the African plate to the south and east of the spreading center (O'Connor & Jokat, 2015; Rohde et al., 2013). The off-axis HIMU magmatism progressed southwestward along the Walvis Ridge, reaching the southern end of Valdivia Bank by ~55 Ma, forming the ridge-like seamounts at DR45 and DR46 (Homrighausen, Hoernle, Geldmacher, et al., 2018). At about the same time, the Tristan-Gough plume splits, forming two, compositionally distinct plume tracks, and ultimately generating the Guyot Province to the southwest (Figure 11c).

With the Tristan-Gough plume now stranded beneath the African plate to the south, the situation in the region of the SAT is quite different from that along the Walvis Ridge. Although magnetic anomaly patterns over this period of time are complicated, there is general agreement that by ~65 Ma several ridge jumps occurred to the west of the Walvis Ridge (Graça et al., 2019; Rohde et al., 2013; Sager et al., 2021; Thoram et al., 2019). Crust and mantle lithosphere previously belonging to the African plate were transferred to the South American plate by these events (Figures 11b and 11c). Our observations from the SAT basalts suggest that it also led to relocation of the spreading axis over the leading edge of the HIMU plume (Figures 11c and 11d), which had been migrating westward through the shallow asthenosphere beneath the African oceanic lithosphere in the direction of prevailing mantle flow (Figure 10c). As a result, the mantle beneath the spreading center was no longer a typical MORB-source mantle, but rather the remains of the HIMU plume that had previously melted to give rise to the late-stage, off-axis volcanism along the Walvis Ridge. Were it not for the ridge jump(s) and associated mantle upwelling, the previously melted plume stem would likely have remained below the solidus and further melting would not have occurred.

This scenario provides an explanation not only for the presence of HIMU signatures in the 61 Ma SAT basalts but also for the unusual magmatic stratigraphy at Site U1556, which is MORB-like at the bottom and OIB-like at the top. It can also account for the existence of anomalously thin crust, indicative of underlying mantle that is either colder or more depleted (or both) than normal MORB-source mantle. Mechanistically, this can be related to the structure and melting dynamics of a non-vertical plume, as proposed by Hofmann and Farnetani (2013). Their model accounts for the depth and degree of melting of anhydrous peridotite along three-dimensional flow trajectories in a dynamic, non-vertical plume. The model was developed to explain the compositions of rejuvenated-stage volcanism along the Hawaiian seamount chain, which is magmatism that occurs 1–2 Myr after the main shield stage volcanism and once the oceanic plate has moved away from the main plume stem. While the

15252027, 2025, 4, Downloaded from https://agupubs.onlinelibrary.wiley.com/doi/10.1029/2025GC012175 by British Geological Survey, Wiley Online Library on [19/05/2025]. See the Terms and Conditions (https://onlinelibrary.wiley.com/terms-and-conditions) on Wiley Online Library for rules of use; OA articles are governed by the applicable Creative Commons License

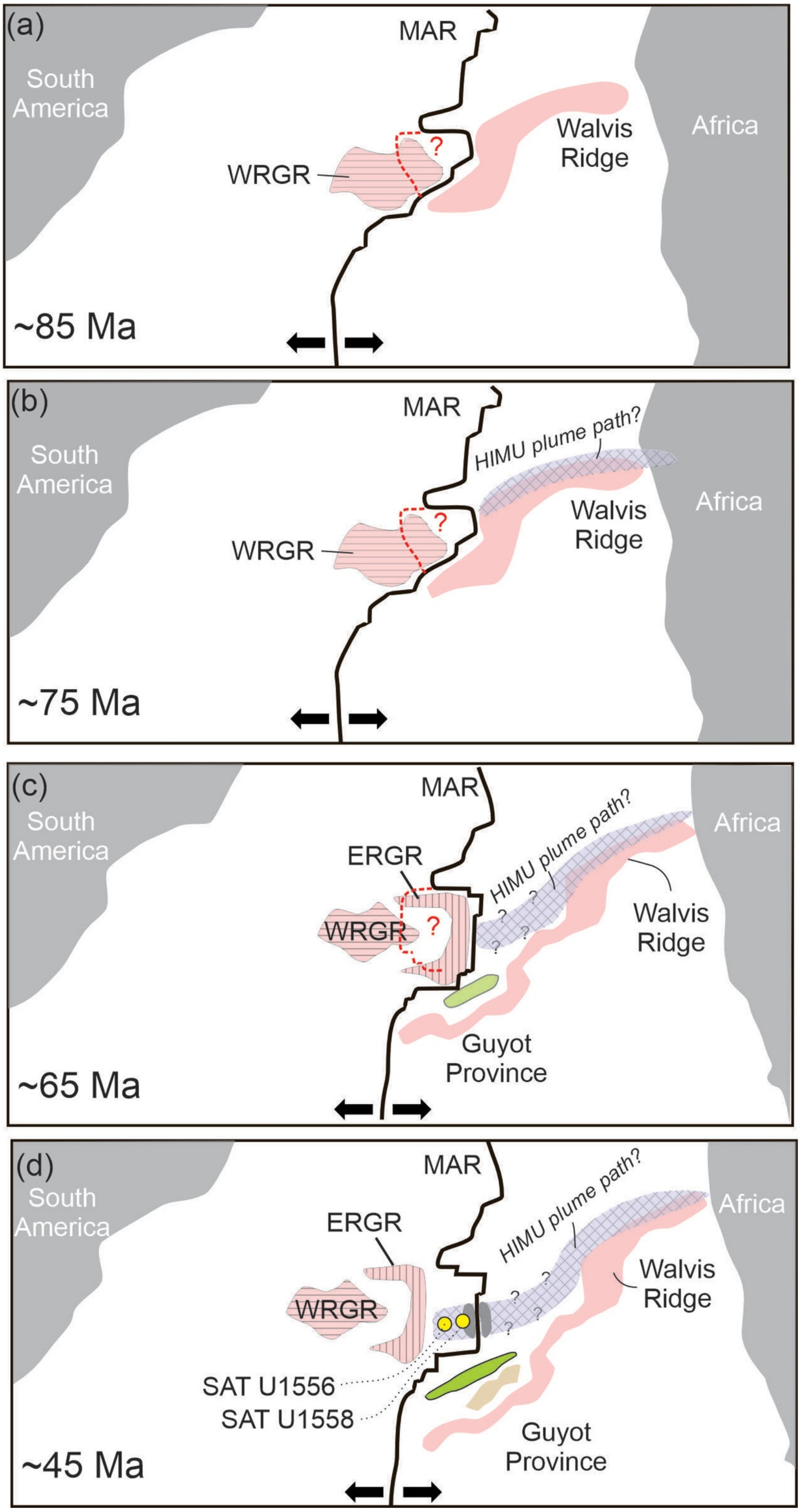

Figure 11.

15252027, 2025, 4, Downloaded from https://agupubs.onlinelibrary.wiley.com/doi/10.1029/2025GC012175 by British Geological Survey, Wiley Online Library on [19/05/2025]. See the Terms and Conditions (https://onlinelibrary.wiley.com/terms-and-conditions) on Wiley Online Library for rules of use; OA articles are governed by the applicable Creative Commons License

geodynamic setting is different, the general principles are similar and can be applied in a qualitative manner to the SAT–Walvis setting.

An adaptation of the Hofmann and Farnetani (2013) model is shown in Figure 12. The ascending plume crosses the solidus at a depth determined by the plume's potential temperature and composition (particularly volatile content). Because the plume is decompressing and assumed to be fertile on ascent, the potential for melting will be greatest at this early stage, depleting this portion of the plume (denoted as the High Melting Region, HMR, on Figures 12a and 12b). The ascending plume intersects the continental lithosphere and is deflected—in the case of the SAT-Walvis HIMU plume, it flows westward (via "upside down drainage") toward the South Atlantic Ocean basin. This changes the configuration of the melting regime relative to that of a vertical plume stem. In particular, the plume stem can now be considered to have an upper portion and a lower portion. The upper portion is relatively depleted due to melt extraction from within the high melting region (HMR), although it may still be able to produce some melt within the Low Melting Region (LMR, Figures 12a and 12b) if it upwells to shallow enough depths that it crosses the solidus again. However, the melts generated will be less enriched in incompatible elements (including Nd, Hf, Sr, and Pb) because of previous melting in the HMR. The lowermost part of the plume is less depleted, since it has been subjected to little or no melt extraction, because it remained below the solidus in the non-vertical plume configuration; the bend in the plume prevents it from ascending to shallow enough depths to cross the solidus (Figure 12a). As such, it retains the capacity to produce melts that are enriched in incompatible elements.

An interesting feature of the Hofmann and Farnetani (2013) model is the recognition of the need for a peripheral sheath of depleted material surrounding the plume stem that underwent that depletion sometime in the distant past (Figure 12). This is similar to the structure for the Iceland plume proposed by Kempton et al. (2000) to explain some of the isotopically depleted compositions observed on Iceland and the Reykjanes Ridge. Hofmann and Farnetani (2013) attribute this material to entrainment of ambient deep mantle, sourced from the thermal boundary layer near the source of the main plume; this material is believed to be depleted relative to estimates of primitive mantle, possibly in response to segregation of an early enriched reservoir (Boyet & Carlson, 2005; Kondo et al., 2016). Regardless, the presence of an ancient, depleted sheath surrounding the plume stem appears to be a common feature of several plume models (Hoernle et al., 2015; Hofmann & Farnetani, 2013; Kempton et al., 2000).

As a result of the ridge jump(s) west of the Walvis Ridge (Figures 11c and 11d), thinning of the oceanic lithosphere allows the partially depleted plume to upwell to shallow depths beneath the spreading center (Figures 10c and 12b), which facilitates partial melting. The cartoon in Figure 12c shows how sampling of the non-vertical plume stem, variably depleted by the complex melting regime and history, could give rise to the unusual magmatic stratigraphy of Site U1556. In particular, the first material to reach depths shallow enough to melt is the plume sheath. As explained above, this material, believed to be derived from the ambient deep mantle, has an isotopic composition indicative of long-term, time-integrated depletion. For the 61 Ma SAT basalts, this corresponds to the tholeiites of U1556 SSC and U1557, the high εHf and ^{207}Pb/^{204}Pb isotopic ratios of which indicate a depleted source requiring long-term isolation from the convecting upper mantle. Because this material is already depleted, it is not able to generate large volumes of melt, hence the thinner-than-normal crust at Site U1556. The trace element patterns for these basalts, however, indicate recent re-enrichment prior to melt generation (Figures 4e, 4f, and 8); indeed, it may be, in part, a contribution of volatile-rich melts derived from the underlying plume stem that facilitates partial melting in the depleted sheath.

Figure 11. Cartoon showing evolution and reorganization of the mid-Atlantic Ridge (MAR) spreading center between ∼85 and 45 Ma, formation of the Rio Grande Rise and Walvis Ridge, and appearance of the HIMU plume; adapted from Sager et al. (2021) and Hoyer et al. (2022). An approximate age for each panel is given in the lower left corner. Heavy lines indicate active spreading ridges; black arrows indicate the direction of seafloor spreading at the MAR. Dashed lines denote abandoned spreading ridges; in panels (a–c) they indicate the western boundary of the microplate proposed by Sager et al. (2021). (a) At ∼85 Ma, the Tristan-Gough plume is ridge-centered, forming the Western Rio Grande Rise and Walvis Ridge. (b) By ∼75 Ma, the HIMU plume arrives beneath the Walvis Ridge, giving rise to the late-stage, off-axis HIMU volcanism near the coast of Africa (Homrighausen, Hoernle, Geldmacher, et al., 2018). The Tristan-Gough plume migrates southward and continues to interact with the spreading center, forming the eastern Rio Grande Rise (ERGR) (Homrighausen et al., 2020). (c) By ∼65 Ma, after one or more ridge jumps and migration of the spreading center, the Tristan-Gough plume stem is isolated within the African plate and formation of the ERGR ceases. We hypothesize that the HIMU plume material is either nearby or captured by the ridge axis around this time. (d) By 45 Ma, spreading at the ridge axis has largely replaced the HIMU plume material with a more typical MORB-source mantle (dark gray bands on each side of the ridge axis), isolating a fragment of HIMU-influenced mantle on the South American plate, as sampled at IODP Site U1556. Site U1558 records the transition back to the NMORB source mantle in the region of the South Atlantic Transect.

15252027, 2025, 4, Downloaded from https://agupubs.onlinelibrary.wiley.com/doi/10.1029/2025GC012175 by British Geological Survey, Wiley Online Library on [19/05/2025]. See the Terms and Conditions (https://onlinelibrary.wiley.com/terms-and-conditions) on Wiley Online Library for rules of use; OA articles are governed by the applicable Creative Commons License

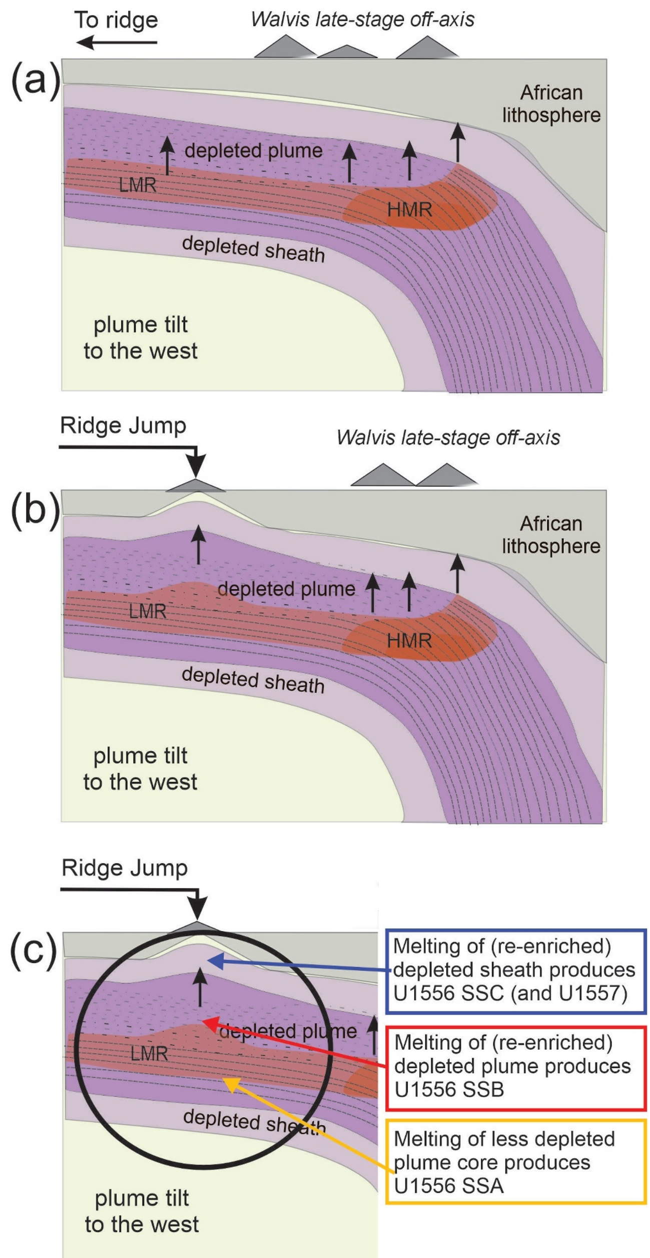

Figure 12. (a) Adaptation of the numerical model of Hofmann and Farnetani (2013) for partial melting in a dynamic, non-vertical plume. Solid flow path for the plume prior to melting indicated by the dashed black lines. Region of melting shown in red. Peridotite, depleted by melt extraction, denoted by dot-dash gray lines. Downstream from the high melting region, partial melting remains possible in the low melting region (LMR), but the only fertile regions lie within the underside of the plume. The sheath surrounding the plume stem is depleted material entrained from the ambient lower mantle. (b) In the SAT scenario, Site U1556, ridge jumps relocate the spreading center over the non-vertical plume steam, leading to upwelling of the plume mantle to shallow levels, which enables further melting at shallow depths. (c) Proposal for the types of melts generated from each region of the non-vertical plume beneath the spreading center and how each relates to the stratigraphy of Site U1556. The first melts out, that is, U1556 SSC, are produced by melting of the plume sheath, with its isotopic evidence for ancient depletion but trace element abundances indicating recent partial re-enrichment. With continued upwelling, the plume stem, previously depleted by having produced the older, late-stage, off-axis volcanism associated with the Walvis Ridge (Homrighausen, Hoernle, Geldmacher, et al., 2018), crosses the solidus, producing U1556 SSB. Finally, the region on the underside of the plume, which still retains some of the enriched plume material, melts to give rise to U1556 SSA alkali basalts.

15252027, 2025, 4, Downloaded from https://agupubs.onlinelibrary.wiley.com/doi/10.1029/2025GC012175 by British Geological Survey, Wiley Online Library on [19/05/2025]. See the Terms and Conditions (https://onlinelibrary.wiley.com/terms-and-conditions) on Wiley Online Library for rules of use; OA articles are governed by the applicable Creative Commons License

10.1029/2025GC012175

15252027, 2025, 4, Downloaded from https://agupubs.onlinelibrary.wiley.com/doi/10.1029/2025GC012175 by British Geological Survey, Wiley Online Library on [19/05/2025]. See the Terms and Conditions (https://onlinelibrary.wiley.com/terms-and-conditions) on Wiley Online Library for rules of use; OA articles are governed by the applicable Creative Commons License

With continued upwelling at the new ridge axis, the depleted plume sheath is replaced by the less depleted plume stem, the melting of which generates U1556 SSB enriched tholeiites. Finally, relatively undepleted plume stem material upwells sufficiently to cross the solidus, giving rise to U1556 SSA basalts. Thus, the magmatic stratigraphy at Site U1556 can be explained by the top-down sequential tapping of an inclined plume source, with the top-to-bottom depletion-to-enrichment structure of this source reflected in reversed stratigraphic order (Figure 12c).

Over time, continued spreading, and mantle upwelling, removed the captured plume stem from beneath the ridge, replacing it with a typical MORB-source mantle from the underlying convecting asthenosphere (Figure 11d). The change in isotopic and trace element compositions along the SAT (Figures 4–12) indicate that this occurs by ∼49.2 Ma when the basalts of Site U1558 formed, after which time the system remains sourced from the shallow asthenosphere (MORB-source mantle). This time frame is consistent with the slow upwelling rates observed for Sites U1556 and U1558 (13–20 mm/yr half rate). At these rates, a plume stem roughly 150–200 km in diameter (Koppers et al., 2021) could be replaced from beneath the ridge system within ∼12 Myr.

5. Summary

1. Basaltic basement, ranging from 61.2 to 6.6 Ma, was recovered from a transect of seven drill sites on the western flank of the MAR at ∼31°S. The four youngest sites (≤49.2 Ma) consist of MORB tholeiites depleted in incompatible trace elements relative to NMORB (Gale et al., 2013) but similar to MORBs from the current ridge axis between 25° and 28°S. The data suggest that the convecting asthenosphere beneath this region of the South Atlantic includes a significant component that is relatively free of re-enrichment by mantle plumes and is more depleted than NMORB-source mantle globally.
2. The basement stratigraphy recovered from the oldest SAT site (U1556; 61.2 Ma), located ∼200 km east of the ERGR, is more complex than that of the younger sites, ranging from MORB-like tholeiites at the bottom of the hole to OIB-like alkali basalts at the top. The U1556 basalts, along with basalt clasts from the talus breccias at Site U1557 (60.7 Ma), are also isotopically distinct. Their Pb-Nd-Hf isotope systematics indicate the presence of a HIMU plume component in the MAR mantle source at the time of emplacement. Thus, our new isotope results provide the first evidence for a HIMU component beneath the South American plate in a region where the plume component was previously inferred to be entirely from the EMI-type Tristan-Gough plume system.
3. The presence of a HIMU component in this location is the consequence of one or more ridge jumps that occurred west of the Walvis Ridge at around 65 Ma. This event transferred not only crust and mantle lithosphere from the African plate to the South American plate but also relocated the spreading axis over a portion of the HIMU plume that had previously given rise to the late-stage, off-axis HIMU magmatism observed on and adjacent to the Walvis Ridge.
4. The complex structure of the melting regime in the non-vertical plume stem led to variable depletion by melt extraction that left the upper portions more depleted than deeper sections. Upwelling beneath the spreading center progressively tapped this variably depleted source, reproducing it in reverse in the magmatic stratigraphy at Site U1556, generating isotopically depleted tholeiites, which occur at the bottom, and enriched alkali basalts at the top. Based on the upwelling rates inferred for Sites U1556 and U1558 (13–20 mm/yr half rate), a plume stem roughly 150–200 km in diameter could be replaced from beneath the ridge system within ∼12 Myr, consistent with the loss of the HIMU signature by the time of Site U1558 (49.2 Ma).

Acknowledgments

This research used samples and/or data provided by the International Ocean Discovery Program (IODP). The authors would like to recognize the excellent support from IODP, the JOIDES Resolution Facility, and the scientific staff and crew aboard the JOIDES Resolution during Expeditions 390/393, as well as all Shipboard Scientists not included in this study. This research would not have been possible without their contributions. Funding support to U.S. participant Pamela Kempton IODP Expedition 390 Post-Expedition Activity Award from the United States Science Support Program (USSSP) is gratefully acknowledged. Support from Royal Society URF award to RMC (URF\R1\180320 and URF\R\231021) and UKRI NERC UK IODP Moratorium awards NE/X0001X/1 to RMC, NE/X009440/1 to DAHT, NE/X00631X/1 to ADE and DAHT, and NE/X003485/1 to TMB and DAHT are also gratefully acknowledged. EA acknowledges support from the Alexander von Humboldt Foundation. Constructive reviews were provided by Dr. David Peate and an anonymous reviewer. We would also like to thank Dr. Jacqueline Dixon for her efficient editorial handling.

Data Availability Statement

All data in Tables S1-S3 (major elements and trace elements, isotopes, and standard data) used in the study are available from the Kansas State University Research Exchange (K-Rex) via https://hdl.handle.net/2097/44803.

References

Agranier, A., Blichert-Toft, J., Graham, D., Debaille, V., Schiano, P., & Albarède, F. (2005). The spectra of isotopic heterogeneities along the mid-Atlantic Ridge. *Earth and Planetary Science Letters*, *238*(1–2), 96–109. https://doi.org/10.1016/j.epsl.2005.07.011

Andres, M., Blichert-Toft, J., & Shilling, J.-G. (2004). Nature of the depleted upper mantle beneath the Atlantic: Evidence from Hf isotopes in normal mid-ocean ridge basalts from 79°N to 55°S. *Earth and Planetary Science Letters*, *225*, 89–103. https://doi.org/10.1016/j.epsl.2004.05.041

Boyet, M., & Carlson, R. W. (2005). ^{142}Nd evidence for early (>4.53 Ga) global differentiation of the silicate Earth. *Science*, *309*, 576–581. https://doi.org/10.1126/science.111363

Burke, K., Steinberger, B., Torsvik, T. H., & Smethurst, M. A. (2008). Plume generation zones at the margins of large low shear velocity provinces on the core-mantle boundary. *Earth and Planetary Science Letters*, *265*(1–2), 49–60. https://doi.org/10.1016/j.epsl.2007.09.042

Chauvel, C., Lewin, E., Carpentier, M., Arndt, N. T., & Marini, J.-C. (2008). Role of recycled oceanic basalt and sediment in generating the Hf-Nd mantle array. *Nature Geoscience*, *1*, 64–67. https://doi.org/10.1038/ngeo.2007.51

Christeson, G. L., Reece, R. S., Kardell, D. A., Estep, J. D., Fedotova, A., & Goff, J. A. (2020). South Atlantic Transect: Variations in oceanic crustal structure at 31°S. *Geochemistry, Geophysics, Geosystems*, *21*(7), e2020GC009017. https://doi.org/10.1029/2020GC009017

Class, C., Davidson, P. C., Koppers, A. P., & Sager, W. (2023). On/near ridge formation of the Eastern Rio Grande Rise, South Atlantic. In *Paper presented at 2023 Goldschmidt Conference, Paper 17326*. Retrieved from https://conf.goldschmidt.info/goldschmidt/2023/meetingapp.cgi/Paper/17326

Class, C., & Lehnert, K. (2012). *PetDB Expert MORB (Mid-Ocean Ridge Basalt) Compilation, Version 1.0*. Interdisciplinary Earth Data Alliance (IEDA). https://doi.org/10.1594/IEDA/100060

Class, C., & le Roex, A. (2011). South Atlantic DUPAL anomaly—Dynamic and compositional evidence against a recent shallow origin. *Earth and Planetary Science Letters*, *305*(1–2), 92–102. https://doi.org/10.1016/j.epsl.2011.02.036

Cliff, R. A., Baker, P. E., & Mateer, N. J. (1991). Geochemistry of inaccessible island volcanics. *Chemical Geology*, *92*(4), 251–260. https://doi.org/10.1016/0009-2541(91)90073-Z

Coggon, R. M., Teagle, D. A. H., Sylvan, J. B., Reece, J., Estes, E. R., Williams, T. J., et al. (2024). *Proceedings of the International Ocean Discovery Program, Volume 390/393, South Atlantic Transect*. International Ocean Discovery Program. https://doi.org/10.14379/iodp.proc.390393.103.2024

Colli, L., Stotz, I., Bunge, H.-P., Smethurst, M., Clark, S., Iaffaldano, G., et al. (2014). Rapid South Atlantic spreading changes and coeval vertical motion in surrounding continents: Evidence for temporal changes of pressure-driven upper mantle flow. *Tectonics*, *32*(7), 1304–1321. https://doi.org/10.1002/2014TC003612

Davidson, P., Class, C., Arden, S., Koppers, A., Sager, W., & Bolge, L. (2023). Far-field seamounts related to the Tristan-Gough mantle plume extend from the Rio Grande Rise to the Mid-Atlantic Ridge. In *Paper presented at 2023 AGU Fall Meeting, San Francisco, CA, Poster No. 0289, 2023AGUFM.T43D0289D*.

Doucet, S., Weis, D., Scoates, J. S., Nicolaysen, K., Frey, F. A., & Giret, A. (2002). The depleted mantle component in Kerguelen Archipelago basalts: Petrogenesis of tholeiitic–Transitional basalts from the Loranchet Peninsula. *Journal of Petrology*, *43*(7), 1341–1366. https://doi.org/10.1093/petrology/43.7.1341

Douglass, J., & Schilling, J.-G. (2000). Systematics of three-component, pseudo-binary mixing lines in 2D isotope ratio space: Representations and implications for mantle plume–ridge interaction. *Chemical Geology*, *163*(1–4), 1–23. https://doi.org/10.1016/S0009-2541(99)00070-4

Douglass, J., Schilling, J.-G., & Fontignie, D. (1999). Plume–ridge interactions of the Discovery and Shona mantle plumes with the southern Mid–Atlantic Ridge (40–55°S). *Journal of Geophysical Research*, *104*(B2), 2941–2962. https://doi.org/10.1029/98JB02642

Fitton, J. G., Saunders, A. D., Norry, M. J., Hardarson, B. S., & Taylor, R. N. (1997). Thermal and chemical structure of the Iceland plume. *Earth and Planetary Science Letters*, *153*(3–4), 197–208. https://doi.org/10.1016/S0012-821X(97)00170-2

Fontignie, D., & Schilling, J.-G. (1996). Mantle heterogeneities beneath the South Atlantic: A Nd–Sr–Pb isotope study along the Mid–Atlantic Ridge (3°S–46°S). *Earth and Planetary Science Letters*, *142*(1–2), 209–221. https://doi.org/10.1016/0012-821X(96)00079-9

French, S. W., & Romanowicz, B. (2015). Broad plumes rooted at the base of the Earth's mantle beneath major hotspots. *Nature*, *525*(7567), 95–99. https://doi.org/10.1038/nature14876

Fromm, T., Planert, L., Jokat, W., Ryberg, T., Behrmann, J. H., Weber, M. H., & Haberlands, C. (2015). South Atlantic opening: A plume-induced breakup? *Geology*, *43*(10), 931–934. https://doi.org/10.1130/G36936.1

Gale, A., Dalton, C. A., Langmuir, C. H., Su, Y., & Schilling, J.-G. (2013). The mean composition of ocean ridge basalts. *Geochemistry, Geophysics, Geosystems*, *14*(3), 489–518. https://doi.org/10.1029/2012GC004334

Garcia, M. A., Weis, D., Jicha, B. R., Ito, G., & Hanano, D. (2016). Petrology and geochronology of lavas from Ka'ula Volcano: Implications for rejuvenated volcanism of the Hawaiian mantle plume. *Geochimica et Cosmochimica Acta*, *185*, 278–301. https://doi.org/10.1016/j.gca.2016.03.025

Gassmöller, R., Dannberg, J., Bredow, E., Steinberger, B., & Torsvik, T. H. (2016). Major influence of plume-ridge interaction, lithosphere thickness variations, and global mantle flow on hotspot volcanism—The example of Tristan. *Geochemistry, Geophysics, Geosystems*, *17*(4), 1454–1479. https://doi.org/10.1002/2015GC006177

GEBCO Compilation Group. (2024). GEBCO 2024 Grid. https://doi.org/10.5285/1c44ce99-0a0d-5f4f-e063-7086abc0ea0f

Gibson, S. A., Thompson, R. N., Day, J. A., Humphris, S. E., & Dickin, A. P. (2005). Melt generation processes associated with the Tristan mantle plume: Constraints on the origin of EM-1. *Earth and Planetary Science Letters*, *237*(3–4), 744–767. https://doi.org/10.1016/j.epsl.2005.06.015

Graça, M. C., Kusznirc, N., & Stanton, N. S. G. (2019). Crustal thickness mapping of the central South Atlantic and the geodynamic development of the Rio Grande Rise and Walvis Ridge. *Marine and Petroleum Geology*, *101*, 230–242. https://doi.org/10.1016/j.marpetgeo.2018.12.011

Harpp, K. S., & Weis, D. (2020). Insights into the origins and compositions of mantle plumes: A comparison of Galápagos and Hawai'i. *Geochemistry, Geophysics, Geosystems*, *21*(9), e2019GC008887. https://doi.org/10.1029/2019GC008887

Harrison, L. N., Weis, D., & Garcia, M. O. (2020). The multiple depleted mantle components in the Hawaiian-Emperor chain. *Chemical Geology*, *532*, 119324. https://doi.org/10.1016/j.chemgeo.2019.119324

Hart, S. R. (1984). A large scale isotope anomaly in the southern hemisphere mantle. *Nature*, *309*(5971), 753–757. https://doi.org/10.1038/309753a0

Hoernle, K., Rohde, J., Hauff, F., Garbe- Schönberg, D., Homrighausen, S., Werner, R., & Morgan, J. P. (2015). How and when plume zonation appeared during the 132 Myr evolution of the Tristan Hotspot. *Nature Communications*, *6*(1), 7799. https://doi.org/10.1038/ncomms8799

Hofmann, A. W., & Farnetani, C. G. (2013). Two views of Hawaiian plume structure. *Geochemistry, Geophysics, Geosystems*, *14*(12), 5308–5322. https://doi.org/10.1002/2013GC004942

Homrighausen, S., Hoernle, K., Geldmacher, J., Wartho, J.-A., Hauff, F., Portnyagin, M., et al. (2018). Unexpected HIMU-type late-stage volcanism on the Walvis Ridge. *Earth and Planetary Science Letters*, *492*, 251–263. https://doi.org/10.1016/j.epsl.2018.03.049

Homrighausen, S., Hoernle, K., Hauff, F., Geldmacher, J., Wartho, J.-A., van den Bogaard, P., & Garbe-Schönberg, D. (2018). Global distribution of the HIMU end member: Formation through Archean plume-lid tectonics. *Earth-Science Reviews*, *182*, 85–101. https://doi.org/10.1016/j.earscirev.2018.04.009

Homrighausen, S., Hoernle, K., Hauff, F., Hoyer, P. A., Haase, K. M., Geissler, W. H., & Geldmacher, J. (2023). Evidence for compositionally distinct upper mantle plumelets since the early history of the Tristan-Gough hotspot. *Nature Communications*, *14*(1), 3908. https://doi.org/10.1038/s41467-023-39585-0

15252027, 2025, 4, Downloaded from https://agupubs.onlinelibrary.wiley.com/doi/10.1029/2025GC012175 by British Geological Survey, Wiley Online Library on [19/05/2025]. See the Terms and Conditions (https://onlinelibrary.wiley.com/terms-and-conditions) on Wiley Online Library for rules of use; OA articles are governed by the applicable Creative Commons License

Homrighausen, S., Hoernle, K., Hauff, F., Wartho, J.-A., Garbe-Schönberg, C. D., & Garbe-Schönberg, D. (2019). New age and geochemical data from the Walvis Ridge: The temporal and spatial diversity of South Atlantic intraplate volcanism and its possible origin. *Geochemica et Cosmochimica Acta*, *245*, 16–34. https://doi.org/10.1016/j.gca.2018.09.002

Homrighausen, S., Hoernle, K., Zhou, H., Geldmacher, J., Wartho, J.-A., Hauff, F., et al. (2020). Paired EMI-HIMU hotspots in the South Atlantic—Starting plume heads trigger compositionally distinct secondary plumes? *Science Advances*, *6*(28), eaba0282. https://doi.org/10.1126/sciadv.aba0282

Hoyer, P. A., Haase, K. M., Regelous, M., O'Connor, J. M., Homrighausen, S., Geissler, W. H., & Jokat, W. (2022). Mantle plume and rift-related volcanism during the evolution of the Rio Grande Rise. *Nature Communications Earth and Environment*, *3*(1), 18. https://doi.org/10.1038/s43247-022-00349-1

Humphris, S. E., & Thompson, G. (1983). Geochemistry of rare Earth elements in basalts from the Walvis Ridge: Implications for its origin and evolution. *Earth and Planetary Science Letters*, *66*, 223–242. https://doi.org/10.1016/0012-821X(83)90138-3

Jones, R. E., van Keken, P. E., Hauri, E. H., Tuckers, J. M., Vervoort, J., & Ballentine, C. J. (2019). Origins of the terrestrial Hf-Nd mantle array: Evidence from a combined geodynamical-geochemical approach. *Earth and Planetary Science Letters*, *518*, 26–39. https://doi.org/10.1016/j.epsl.2019.04.015

Jonnalagadda, M., Belgrano, T., Ryan, J., Kempton, P., Evans, A., Grant, L., et al. (2024). Data report: High downhole resolution portable XRF geochemistry of South Atlantic Transect basement cores, IODP Expeditions 390C, 395E, 390 and 393. In *Proceedings of the International Ocean Discovery Program* (Vol. 390/393). https://doi.org/10.14379/iodp.proc.390393.210.2024

Kardell, D. A., Christeson, G. L., Estep, J. D., Reece, R. S., & Carlson, R. L. (2019). Long-lasting evolution of Layer 2A in the western South Atlantic: Evidence for low-temperature hydrothermal circulation in old oceanic crust. *Journal of Geophysical Research: Solid Earth*, *124*(3), 2252–2273. https://doi.org/10.1029/2018JB016925

Kempton, P. D., Nowell, G. M., Fitton, J. G., Saunders, A. D., Taylor, R. N., Hardarson, B., & Pearson, G. (2000). The Iceland plume in space and time: A Sr-Nd-Pb-Hf study of the North Atlantic rifted margin. *Earth and Planetary Science Letters*, *177*(3–4), 255–271. https://doi.org/10.1016/S0012-821X(00)00047-9

Kondo, N., Yoshino, T., Matsukage, K. N., & Kogiso, T. (2016). Major element composition of an Early Enriched Reservoir: Constraints from ^{142}Nd/^{144}Nd isotope systematics. *Progress in Earth and Planetary Science*, *3*(1), 25. https://doi.org/10.1186/s40645-016-0099-0

Koppers, A. P., Becker, T., Jackson, M. G., Konrad, K., Müller, D., Romanowicz, B., et al. (2021). Mantle plumes and their role in Earth processes. *Nature Reviews Earth & Environment*, *2*(6), 1–20. https://doi.org/10.1038/s43017-021-00168-6

le Roex, A. P., Cliff, R. A., & Adair, J. I. (1990). Tristan da Cunha, South Atlantic: Geochemistry and petrogenesis of a basanite–phonolite lava series. *Journal of Petrology*, *31*(4), 779–812. https://doi.org/10.1093/petrology/31.4.779

Li, C., Zhang, H., Guan, Y., Zhu, A., & Shi, X. (2023). South Mid-Atlantic Ridge 25.3–27.7°S segment basalts: Implications for entrainment of the Tristan plume material in the mid-ocean ridge system. *Chemical Geology*, *640*, 121743. https://doi.org/10.1016/j.chemgeo.2023.121743

Macdonald, G. A., & Katsura, T. (1964). Chemical composition of Hawaiian lavas. *Journal of Petrology*, *5*(1), 82–133. https://doi.org/10.1093/petrology/5.1.82

Maxwell, A. E., Von Herzen, R., & Shipboard Scientists. (1970). *Initial Reports of the Deep Sea Drilling Project, v. 3*. U.S. Government Printing Office. https://doi.org/10.2973/dsdp.proc.3.1970

Miyashiro, A. (1978). Nature of alkalic volcanic rock series. *Contributions to Mineralogy and Petrology*, *66*(1), 91–104. https://doi.org/10.1007/bf00376089

Mohriak, W., Nóbrega, M., Odegard, M., Gomes, B., & Dickson, W. (2010). Geological and geophysical interpretation of the Rio Grande Rise, south-eastern Brazilian margin: Extensional tectonics and rifting of continental and oceanic crusts. *Petroleum Geoscience*, *16*(3), 231–245. https://doi.org/10.1144/1354-079309-910

Morgan, W. J. (1971). Convection plumes in the lower mantle. *Nature*, *230*(5288), 42–43. https://doi.org/10.1038/230042a0

Niu, Y. (2020). On the cause of continental breakup: A simple analysis in terms of driving mechanisms of plate tectonics and mantle plumes. *Journal of Asian Earth Science*, *194*, 104367. https://doi.org/10.1016/j.jseaes.2020.104367

O'Connor, J. M., & Jokat, W. (2015). Age distribution of Ocean Drill sites across the Central Walvis Ridge indicates plate boundary control of plume volcanism in the South Atlantic. *Earth and Planetary Science Letters*, *424*, 179–190. https://doi.org/10.1016/j.epsl.2015.05.021

Pandey, S., Yuan, X., Debayle, E., Geissler, W. H., & Heit, B. (2022). Plume-lithosphere interaction beneath southwestern Africa – Insights from multi-mode Rayleigh wave tomography. *Tectonophysics*, *842*, 229587. https://doi.org/10.1016/j.tecto.2022.229587

Pearce, J. A. (2008). Geochemical fingerprinting of oceanic basalts with applications to ophiolite classification and the search for Archean oceanic crust. *Lithos*, *100*(1–4), 14–48. https://doi.org/10.1016/j.lithos.2007.06.016

Peate, D. W. (1997). The Parana-Etendeka Province. In J. J. Mahoney & M. F. Coffin (Eds.), *Large Igneous Provinces: Continental, Oceanic, and Planetary Flood Volcanism* (pp. 217–245). American Geophysical Union. https://doi.org/10.1029/GM100p0217

Regelous, M., Niu, Y., Abouchami, W., & Castillo, P. R. (2009). Shallow origin for South Atlantic Dupal Anomaly from lower continental crust: Geochemical evidence from the Mid-Atlantic Ridge at 26°S. *Lithos*, *112*(1–2), 57–72. https://doi.org/10.1016/j.lithos.2008.10.012

Renne, P. R., Glen, J. M., Milner, S. C., & Duncan, A. R. (1996). Age of Etendeka flood volcanism and associated intrusions in southwestern Africa. *Geology*, *24*(7), 659–662. https://doi.org/10.1130/0091-7613(1996)024<0659:AOEFVA>2.3.CO;2

Richards, M. A., Duncan, R. A., & Courtillot, V. E. (1989). Flood basalts and hot-spot tracks: Plume heads and tails. *Science*, *246*(4926), 103–107. https://doi.org/10.1126/science.246.4926.103

Richardson, S. H., Erlank, A. J., Duncan, A. R., & Reid, D. L. (1982). Correlated Nd, Sr and Pb isotope variation in Walvis Ridge basalts and implications for the evolution of their mantle source. *Earth and Planetary Science Letters*, *59*(2), 327–342. https://doi.org/10.1016/0012-821X(82)90135-2

Rohde, J. K., van den Bogaard, P., Hoernle, K., Hauff, F., & Werner, R. (2013). Evidence for an age progression along the Tristan-Gough volcanic track from new ^{40}Ar/^{39}Ar ages on phenocryst phases. *Tectonophysics*, *604*, 60–71. https://doi.org/10.1016/j.tecto.2012.08.026

Sager, W. W., Thoram, S., Engfer, D. W., Koppers, A. A. P., & Class, C. (2021). Late Cretaceous ridge reorganization, microplate formation, and the evolution of the Rio Grande Rise – Walvis Ridge hot spot twins, South Atlantic Ocean. *Geochemistry, Geophysics, Geosystems*, *22*(3), e2020GC009390. https://doi.org/10.1029/2020GC009390

Salters, V. J., & Stracke, A. (2004). Composition of the depleted mantle. *Geochemistry, Geophysics, Geosystems*, *5*, Q05B07. https://doi.org/10.1029/2003GC000597

Sanfilippo, A., Salters, V. J. M., Sokolov, S. Y., Peyve, A. A., & Stracke, A. (2021). Ancient refractory asthenosphere revealed by mantle re-melting at the Arctic Mid-Atlantic Ridge. *Earth and Planetary Science Letters*, *566*, 116981. https://doi.org/10.1016/j.epsl.2021.116981

Sani, C., Sanfilippo, A., Peyve, A. A., Genske, F., & Stracke, A. (2023). Earth mantle's isotopic record of progressive chemical depletion. *AGU Advances*, *4*(2), e2022AV000792. https://doi.org/10.1029/2022AV000792

15252027, 2025, 4, Downloaded from https://agupubs.onlinelibrary.wiley.com/doi/10.1029/2025GC012175 by British Geological Survey, Wiley Online Library on [19/05/2025]. See the Terms and Conditions (https://onlinelibrary.wiley.com/terms-and-conditions) on Wiley Online Library for rules of use; OA articles are governed by the applicable Creative Commons License

Santos, R. V., Ganade, C. E., Lacasse, C. M., Costa, I. S. L., Pessanha, I., Frazão, E. P., et al. (2019). Dating Gondwanan continental crust at the Rio Grande Rise, South Atlantic. *Terra Nova*, *31*(5), 424–429. https://doi.org/10.1111/ter.12405

Schilling, J.-G. (1973). Iceland mantle plume: Geochemical study of Reykjanes Ridge. *Nature*, *242*(5400), 565–571. https://doi.org/10.1038/242565a0

Schilling, J.-G., Thompson, G., Kingsley, R., & Humphris, S. (1985). Hotspot–migrating ridge interaction in the South Atlantic. *Nature*, *313*(5999), 187–191. https://doi.org/10.1038/313187a0

Schwindrofska, A., Hoernle, K., Hauff, F., vanden Bogaard, P., Werner, R., & Garbe-Schönberg, D. (2016). Origin of enriched components in the South Atlantic: Evidence from 40Ma geochemical zonation of the Discovery Seamounts. *Earth and Planetary Science Letters*, *441*, 167–177. https://doi.org/10.1016/j.epsl.2016.02.041

Seton, M., Müller, R. D., Zahirovic, S., Gaina, C., Torsvik, T., Shephard, G., et al. (2012). Global continental and ocean basin reconstructions since 200Ma. *Earth-Science Reviews*, *113*(3–4), 212–217. https://doi.org/10.1016/j.earscirev.2012.03.002

Sleep, N. H. (1997). Lateral flow and ponding of starting plume material. *Journal of Geophysical Research*, *102*(B5), 10001–10012. https://doi.org/10.1029/97JB00551

Stracke, A., Genske, F., Berndt, J., & Koornneef, J. M. (2019). Ubiquitous ultra-depleted domains in Earth's mantle. *Nature Geoscience*, *12*(10), 851–855. https://doi.org/10.1038/s41561-019-0446-z

Stracke, A., Willig, M., Genske, F., Beguelin, P., & Todd, E. (2022). Chemical geodynamics insights from a machine learning approach. *Geochemistry, Geophysics, Geosystems*, *23*(10), e2022GC010606. https://doi.org/10.1029/2022GC010606

Sun, S.-S., & McDonough, W. F. (1989). Chemical and isotopic systematics of oceanic basalts: Implications for mantle composition and processes. *Geological Society London, Special Publications*, *42*(1), 313–345. https://doi.org/10.1144/GSL.SP.1989.042.01.19

Taposeea, C. A., Armitage, J. J., & Collier, J. S. (2017). Asthenosphere and lithosphere structure controls on early onset oceanic crust production in the southern South Atlantic. *Tectonophysics*, *716*, 4–20. https://doi.org/10.1016/j.tecto.2016.06.026

Thoram, S., Sager, W. W., & Jokat, W. (2019). Implications of updated magnetic anomalies for the late cretaceous tectonic evolution of Walvis Ridge. *Geophysical Research Letters*, *46*(16), 9474–9482. https://doi.org/10.1029/2019GL083467

Tilhac, R., Begg, G. C., O'Reilly, S. Y., & Griffin, W. L. (2022). A global review of Hf-Nd isotopes: New perspectives on the chicken-and-egg problem of ancient mantle signatures. *Chemical Geology*, *609*, 121039. https://doi.org/10.1016/j.chemgeo.2022.121039

Torsvik, T. H., Rousse, S., Labails, C., & Smethurst, M. A. (2009). A new scheme for the opening of the South Atlantic Ocean and the dissection of an Aptian salt basin. *Geophysical Journal International*, *177*(3), 1315–1333. https://doi.org/10.1111/j.1365-246X.2009.04137.x

Torsvik, T. H., Smethurst, M. A., Burke, K., & Steinberger, B. (2006). Large igneous provinces generated from the margins of the large low-velocity provinces in the deep mantle. *Geophysics Journal International*, *167*(3), 1447–1460. https://doi.org/10.1111/j.1365-246X.2006.03158.x

Tucker, J. M., van Keken, P. E., Jones, R. E., & Ballentine, C. J. (2020). A role for subducted oceanic crust in generating the depleted mid-ocean ridge basalt mantle. *Geochemistry, Geophysics, Geosystems*, *21*(8), e2020GC009148. https://doi.org/10.1029/2020GC009148

Ussami, N., Chaves, C. A. M., Marques, L. S., & Ernesto, M. (2013). Origin of the Rio Grande Rise–Walvis Ridge reviewed integrating palaeogeographic reconstruction, isotope geochemistry and flexural modelling. *Geological Society London, Special Publication*, *369*(1), 129–146. https://doi.org/10.1144/SP369.10

Vanderkluysen, L., Mahoney, J. J., Koppers, A. P., Beier, C., Regelous, M., Gee, J. S., & Lonsdale, P. F. (2014). Louisville Seamount Chain: Petrogenetic processes and geochemical evolution of the mantle source. *Geochemistry, Geophysics, Geosystems*, *15*(6), 2380–2400. https://doi.org/10.1002/2014GC005288

Willbold, M., & Stracke, A. (2006). Trace element composition of mantle end-members: Implications for recycling of oceanic and upper and lower continental crust. *Geochemistry, Geophysics, Geosystems*, *7*(4), Q04004. https://doi.org/10.1029/2005GC001005

Workman, R. K., & Hart, S. R. (2005). Major and trace element composition of the depleted MORB Mantle (DMM). *Earth and Planetary Science Letters*, *231*(1–2), 53–72. https://doi.org/10.1016/j.epsl.2004.12.005

Zhou, H., Hoernle, K., Geldmacher, J., Hauff, F., Homrighausen, F., Garbe-Schönberg, D., et al. (2022). A HIMU volcanic belt along the SW African coast (∼83–49 Ma): New geochemical clues to deep mantle dynamics from carbonatite and silica-undersaturated complexes in Namibia. *Lithos*, *430–431*, 106839. https://doi.org/10.1016/j.lithos.2022.106839

References From the Supporting Information

Govindaraju, K. (1994). Compilation of working values and sample description for 383 geostandards. *Geostandards Newsletter, The Journal of Geostandards and Geoanalysis*, *18*(S1), 1–158. https://doi.org/10.1046/j.1365-2494.1998.53202081.x-i1

Jarosewich, E., Nelen, J. A., & Norberg, J. A. (1980). Reference samples for electron microprobe analysis. *Geostandards and Geoanalytical Research*, *4*(1), 43–47. https://doi.org/10.1111/j.1751-908X.1980.tb00273.x

Jochum, K. P., Nohl, W., Herwig, K. I., Lammel, E., Stoll, B., & Hofmann, A. (2007). GeoReM: A new geochemical Database for reference materials and isotopic Standards. *Geostandards and Geoanalytical Research*, *29*(3), 333–338. https://doi.org/10.1111/j.1751-908X.2005.tb00904.x

Jochum, K. P., Weis, U., Schwager, B., Stoll, B., Wilson, S. A., Haug, G. H., et al. (2016). Reference values following ISO guidelines for frequently requested rock reference materials. *Geostandards and Geoanalytical Research*, *40*(3), 333–350. https://doi.org/10.1111/j.1751-908X.2015.00392.x

Jochum, K. P., Willbold, M., Raczek, I., Stoll, B., & Herwig, K. (2005). Chemical Characterisation of the USGS Reference Glasses GSA-1G, GSC-1G, GSD-1G, GSE-1G, BCR-2G, BHVO-2G and BIR-1G Using EPMA, ID-TIMS, ID-ICP-MS and LA-ICP-MS. *Geostandards and Geoanalytical Research*, *29*(3), 285–302. https://doi.org/10.1111/j.1751-908X.2005.tb00901.x

Katz, R. F., Spiegelman, M., & Langmuir, C. H. (2003). A new parameterization of hydrous mantle melting. *Geochemistry, Geophysics, Geosystems*, *4*(9), 1073. https://doi.org/10.1029/2002GC000433

Klemme, S., & O'Neill, H. S. C. (2000). The near-solidus transition from garnet lherzolite to spinel lherzolite. *Contributions to Mineralogy and Petrology*, *138*(3), 237–248. https://doi.org/10.1007/s004100050560

Münker, C., Weyer, S., Scherer, E., & Mezger, K. (2001). Separation of high field strength elements (Nb, Ta, Zr, Hf) and Lu from rock samples for MC-ICPMS measurements. *Geochemistry, Geophysics, Geosystems*, *2*(12), 1064. https://doi.org/10.1029/2001GC000183

Nowell, G. M., & Parrish, R. R. (2001). Simultaneous acquisition of isotope compositions and parent/daughter ratios by non-isotope dilution-mode plasma ionisation multi-collector mass spectrometry (PIMMS). In G. Holland & S. D. Tanner (Eds.), *Plasma Source Mass Spectrometry: The New Millennium* (Vol. 267, pp. 298–310). Royal Society of Chemistry Special Publication. https://doi.org/10.1039/9781847551696-00298

15252027, 2025, 4, Downloaded from https://agupubs.onlinelibrary.wiley.com/doi/10.1029/2025GC012175 by British Geological Survey, Wiley Online Library on [19/05/2025]. See the Terms and Conditions (https://onlinelibrary.wiley.com/terms-and-conditions) on Wiley Online Library for rules of use; OA articles are governed by the applicable Creative Commons License

Tanaka, T., Togashi, S., Kamioka, H., Amakawa, H., Kagami, H., Hamamoto, T., et al. (2000). JNdi-1: A neodymium isotopic reference inconsistency with LaJolla neodymium. *Chemical Geology*, *168*(3–4), 279–281. https://doi.org/10.1016/s0009-2541(00)00198-4

Taylor, R. N., Ishizuka, O., Michalik, A., Milton, J. A., & Croudace, I. W. (2015). Evaluating the precision of Pb isotope measurement by mass spectrometry. *Journal of Analytical Atomic Spectrometry*, *30*(1), 198–213. https://doi.org/10.1039/C4JA00279B

Todt, W., Cliff, R. A., Hanser, A., & Hofmann, A. W. (1996). Evaluation of a ^{202}Pb–^{205}Pb double spike for high precision lead isotope analysis. In A. Basu & S. Hart (Eds.), *Earth Processes: Reading the Isotopic Code (1996)*, *American Geophysical Union Geophysical Monograph* (Vol. 95, pp. 429–437). https://doi.org/10.1029/GM095p0429

Turcotte, D. L., & Schubert, G. (1982). *Geodynamics: Applications of continuum physics to geological problems* (p. 450). Wiley.

Vance, D., & Thirlwall, M. (2002). An assessment of mass discrimination in MC-ICPMS using Nd isotopes. *Chemical Geology*, *185*, 227–240. https://doi.org/10.1016/S0009-2541(01)00402-8

15252027, 2025, 4, Downloaded from https://agupubs.onlinelibrary.wiley.com/doi/10.1029/2025GC012175 by British Geological Survey, Wiley Online Library on [19/05/2025]. See the Terms and Conditions (https://onlinelibrary.wiley.com/terms-and-conditions) on Wiley Online Library for rules of use; OA articles are governed by the applicable Creative Commons License